AIP | Physics of Fluids

Scanning tomographic particle image velocimetry applied to a turbulent jet

T. A. Casey, J. Sakakibara, and S. T. Thoroddsen

Citation: Phys. Fluids **25**, 025102 (2013); doi: 10.1063/1.4790640
View online: http://dx.doi.org/10.1063/1.4790640
View Table of Contents: http://pof.aip.org/resource/1/PHFLE6/v25/i2
Published by the American Institute of Physics.

PHYSICS OF FLUIDS **25**, 025102 (2013)

Scanning tomographic particle image velocimetry applied to a turbulent jet

T. A. Casey,[1] J. Sakakibara,[2] and S. T. Thoroddsen[1,3]
[1]*Division of Physical Sciences and Engineering, King Abdullah University of Science and Technology (KAUST), Thuwal 23955-6900, Saudi Arabia*
[2]*Department of Engineering Mechanics and Energy, University of Tsukuba, Tsukuba 305-8573, Japan*
[3]*Clean Combustion Research Center, King Abdullah University of Science and Technology (KAUST), Thuwal 23955-6900, Saudi Arabia*

(Received 17 June 2012; accepted 3 December 2012; published online 21 February 2013)

We introduce a modified *tomographic PIV* technique using four high-speed video cameras and a scanning pulsed laser-volume. By rapidly illuminating adjacent sub-volumes onto separate video frames, we can resolve a larger total volume of velocity vectors, while retaining good spatial resolution. We demonstrate this technique by performing time-resolved measurements of the turbulent structure of a round jet, using up to 9 adjacent volume slices. In essence this technique resolves more velocity planes in the depth direction by maintaining optimal particle image density and limiting the number of ghost particles. The total measurement volumes contain between 1×10^6 and 3×10^6 velocity vectors calculated from up to 1500 reconstructed depthwise image planes, showing time-resolved evolution of the large-scale vortical structures for a turbulent jet of *Re* up to 10 000. © *2013 American Institute of Physics*. [http://dx.doi.org/10.1063/1.4790640]

I. INTRODUCTION

A. Volumetric measurements of velocity

The recent introduction of Tomographic Particle Image Velocimetry (TPIV) has produced great improvements in the acquisition of volumetric measurements of velocity vector fields.[1–4] Earlier methods, based on *holographic reconstruction*[5,6] required much more elaborate optical setups. Another method, *scanning stereoscopic* PIV,[7,8] is simpler to establish, but its application is limited to low speed flows.

TPIV is rapidly becoming an attractive non-intrusive measurement technique for the analysis of 3D flow structure and has been successfully applied to a variety of configurations including cylinder wakes,[1,9] turbulent boundary layers,[10] turbulent jets[11,12] and homogeneous isotropic turbulence.[13] TPIV extends principles from two-camera stereoscopic PIV fully into three dimensions, through the use of multiple cameras and the inclusion of a volume reconstruction step to invert the measured light intensities at each pixel on the sensors into a 3D image, and thus triangulate their positions in 3D space. The reconstruction is typically solved using an iterative approach,[14] the accuracy of which increases with the number of camera views employed in the experiment. While this step carries a large computational burden, being both memory and processor intensive, the development of tomographic reconstruction algorithms is currently developing at pace.[4,15]

Tomographic PIV typically looks at a thin volume slice through the flow field, containing of the order of 20-40 velocity planes, strategically aligned with the pertinent directions of the flow-field. Herein we introduce a variant of tomographic PIV where we rapidly scan the pulsed illumination volume over a larger spatial extent to allow for an increased number of depthwise planes (Fig. 1). What limits the number of planes in the depth direction is the density of particle images projected onto the sensor. For example, if we use 48×48 voxels for a projected interrogation area on the sensor, without exceeding an optimal seeding density of approximately 0.05 particles-per-pixel (*ppp*), this

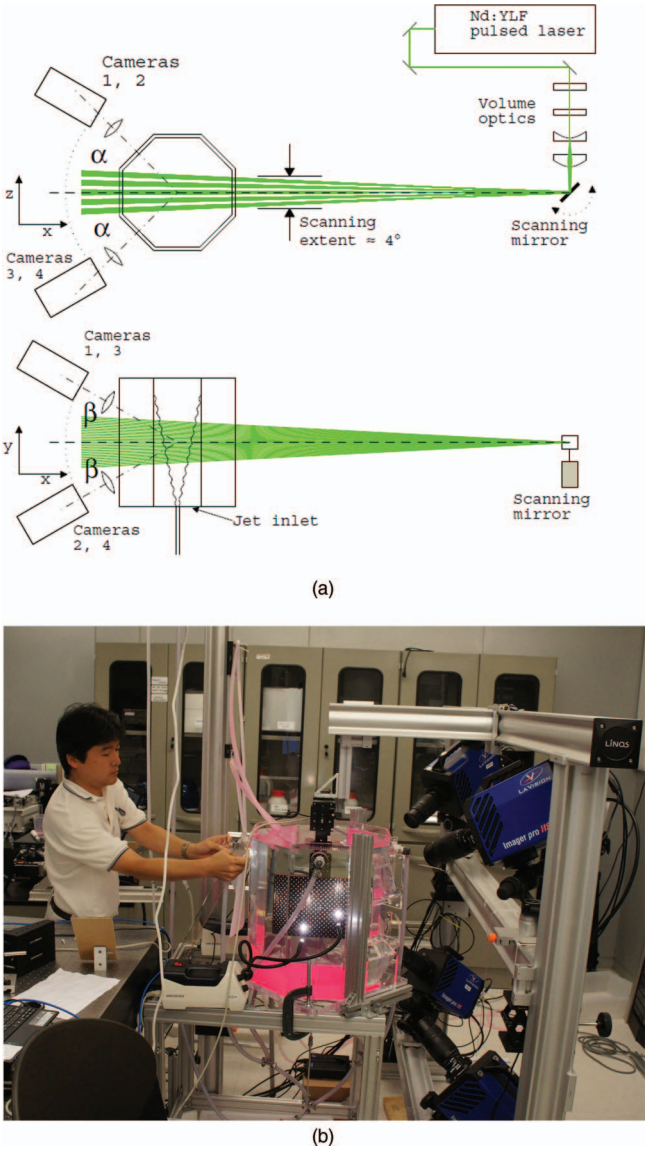

FIG. 1. (a) Sketch of the experimental setup, showing schematically the scanning of the laser volume. (b) Photograph showing the arrangement of the high-speed video cameras and the calibration plate inside the tank. For sharp images the calibration plate is illuminated with four fiber-optic lights. The laser volume illumination shines from the left towards the cameras.

will give 115 particle images available in the entire depth. Using 5 particles in each correlation window for example will thus allow for the use of 23 windows across the depth. By rapidly scanning the illumination volume we can bypass this seeding density based limitation and stack reconstructed planes for a larger spatial extent (Fig. 2).

What limits the seeding density to approximately 0.05 *ppp* in the above argument is the appearance of reconstruction noise, or "ghost particles," during the 3D reconstruction. Ghost particles are generated in the reconstruction due to triangulation ambiguities resulting from the projection of particle positions along each pixel's line of sight. These ghost particles decrease the signal-to-noise ratio of the correlation and their presence can potentially have severe effects on the fine scale fidelity of the correlated vector fields, if they exist in both reconstructions of an image pair. Typically, the

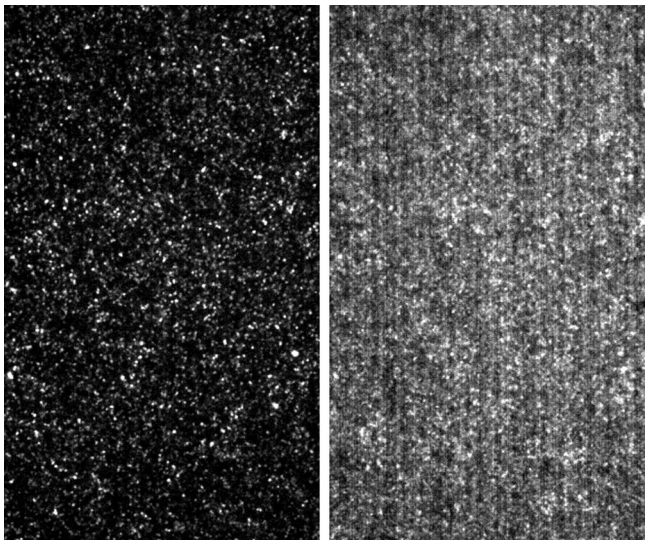

FIG. 2. Comparison of a particle image density from a single illuminated volume (left) and the sum of all 9 volumes (right) acquired using the *double-pulse* protocol. The horizontal extent of each image is approximately 20 mm along the centerline of the jet.

number ratio of ghost to real particles is estimated by[16]

$$N_g = N_p(ppp^{N-1} \cdot A_p^N \cdot L_z), \tag{1}$$

where N is the number of cameras, A_p is the particle image area, L_z is the depthwise extent of the reconstruction volume while N_g and N_p are the number of ghost particles and real particles, respectively. It is apparent that higher seeding density imaged on the sensors (ppp) increases the population of the ghost particles. In addition, the population of ghost particles is proportional to the depth of the illumination volume L_z, even if ppp were kept constant. It can be shown even in a simplified setup that the ghost particle population grows rapidly with increasing light sheet thickness due to the increased illuminated portion of the pixel lines of sight (Fig. 3) which results in increased particle location ambiguity. For this reason TPIV experiments typically avoid large depth domains. Obviously, reduction of the particle number density in the flow field allows for more depth planes without exceeding 0.05 ppp, but at the same time this will limit the overall spatial resolution as larger correlation windows must be employed to ensure that a sufficient number of particles are present in each window to deliver a reasonable correlation peak.

The light source budget, while not usually a critical concern for imaging techniques relying on planar illumination, becomes an important consideration in TPIV where a volume must now be illuminated. Volumetric illumination is achieved by including additional lenses along the beam path, to spread the beam first into a plane and then into a volume, which inevitably results in a large

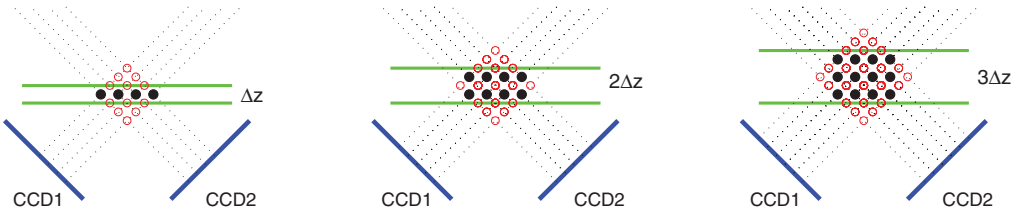

FIG. 3. A simple example of ghost particle population growth with increasing light sheet thickness for a simple 2 camera system with homogeneous seeding density. Black filled circles represent the hypothetical locations of real particles while red hollow circles correspond to locations where ghost particles may be generated due to reconstruction ambiguity.

attenuation of the incident light intensity. Furthermore, since TPIV aims to accurately image the particle positions across the entire illuminated region, large depths of field are required to achieve adequate focus for all the illuminated particles, which is not a stringent requirement for the planar techniques. Therefore, TPIV demands the use of very small apertures on the camera lenses thus increasing the required light intensity that must be supplied by the light source. The requirement for more powerful light sources can be mitigated by employing highly sensitive imaging sensors or intensified sensors (ICCDs) that are tuned for low-light conditions. An alternate approach for increasing the light intensity in a TPIV experiment is to illuminate the experimental volume using multiple passes of a thinner laser volume slice, to amplify the light incident on the seeding particles. This can be achieved by using opposing mirrors to reflect the light, that would otherwise pass unimpeded through the experimental section, back through the experiment a second or more times. Schröder *et al.*[10] employed such a multi-pass light amplification strategy in their investigation of a turbulent boundary layer where approximately 15 adjacent passes of a thick laser sheet were used to illuminate the volume, resulting in an approximately 5 times amplification relative to a single pass with a wider laser sheet. Ghaemi and Scarano[17] achieved a factor of 7 amplification using 14 beam passes in an investigation of the multi-pass illumination approach using smoke particles for seeding. An indirect benefit of employing a scanning strategy to a TPIV investigation is the reduced light intensity required, since the entire experimental volume need not be illuminated at once. The illumination signal is thus amplified by roughly the number of scanning volumes employed.

Kitzhofer and Brücker[18] employed a volumetric scanning method in the context of particle tracking velocimetry (PTV), where the particle densities typically employed are necessarily much lower than those used in TPIV. A laser beam of specified thickness was reflected into their experimental domain using a mirror drum rotating at a constant angular velocity. The illumination of the entire experimental volume was then recorded on a single sensor exposure of each of the three cameras employed and subsequently reconstructed using a pixel line-of-sight technique. In a related PTV work, Kitzhofer *et al.*[19] used the same experimental setup as above but gated the sensors to acquire images for each of 10 scanning volumes. This latter technique is similar to our *fast-scan* mirror protocol where the mirror is scanned as rapidly as possible across the experimental domain, capturing a single image at each mirror location. This technique was successful in reconstructing the particle trajectories induced by a vortex ring but the spatial resolution is still limited by the low seeding densities required for successful particle tracking.

B. Turbulent jet

The round jet is a widely studied canonical turbulent free-shear flow,[20–23] as it is relatively simple to set up experimentally and exhibits self-similar statistical structure, evolving downstream at a constant Reynolds number. An analytical solution of the boundary layer approximation to the incompressible turbulent jet mean momentum equations also exists. This is due to Schlichting[24]and employs a turbulent viscosity closure. Some of our data will be compared to well-established statistical quantities taken from earlier studies, obtained by hot-wires[23] and stereoscopic PIV.[25–27] However, this is not the focus of the paper but is rather done to verify that our experimental configurations adhere to the canonical form. More effort is devoted to demonstrating the potential of this modified technique for extracting time resolved information over a large spatial extent, for example how coherent vortical structures can be identified and tracked in time and their evolution characterized.

TPIV has previously been employed in investigations of the turbulent round jet. Khashehchi *et al.*[11] studied the turbulent/non-turbulent interface in an air jet at $Re = 10\,000$ in a $20 \times 10 \times 3$ mm^3 domain, at 20 inlet diameters downstream of the jet nozzle. The high aspect ratio of their domain reflects the attempt to avoid ghost particle generation. Particle images were acquired using four dual-frame sensors with a relatively high resolution of 8 megapixels (Mpx) but without a temporal dimension as the maximum repeat rate of the cameras was 2 Hz, which is insufficient for resolving the flow evolution in time. The resulting velocity field contained 22 velocity vectors in depth using 50% correlation window overlap indicating approximately 480 reconstructed depthwise planes for the 44^3 voxel (vox) windows employed. The authors used the volumetric data to generate conditional

ensemble statistics of the invariants of the doubly decomposed velocity gradient tensor, as all nine velocity gradients in the domain are deducible from the three-dimensional-three-component(3D, 3C) velocity field. The conditioning parameter chosen was position relative to the interface, thus generating statistics particular to the turbulent and interfacial regions, respectively. The qualitative shape of the joint PDFs of the invariants of the rate of strain and spin tensors in each of these defined regions can give some information about the local flow structure. Correlated behavior of the invariants can imply the existence of coherent structures exhibiting some repeating dynamical behavior, e.g., vortex line stretching or compression.

Staack *et al.*[28] investigated the near field of a turbulent air jet from 0.2 to 15.6 outlet diameters downstream for a $Re = 65\,000$ jet using a $50 \times 50 \times 20\ \text{mm}^3$ measurement domain. Four 4 Mpx sensors with a repeat rate of 4 Hz were employed, operating in dual-frame mode to generate an ensemble for calculating flow statistics. Here 29 vectors in depth were computed using 75% overlap for the 64^3 vox correlation windows used, with 483 reconstructed planes in depth. Despite the inevitable under sampling of spatial flow scales for such a high Reynolds number experiment, the authors were able to reasonably predict the near isotropy of the dissipation rate of turbulence kinetic energy at larger distances from the nozzle. Evidence for the presence of coherent structures was investigated using both two-point correlations and linear stochastic estimations.[29] The autocorrelation of the fluctuating velocity field over a local region centered downstream on the fluid mechanical axis seemed to suggest evidence for asymmetric motions with correlated azimuthal velocity fluctuations. This agrees with the hypothesis that the structures in the downstream are the residuals of azimuthally oriented vortex rings originating from the nozzle that have been deformed to the point of breakdown by strong velocity fluctuations. A more constrained approach to determine the character of coherent structures was employed through a linear stochastic estimation of the velocity field using a relevant constraint. This approach has previously been applied by Matsuda and Sakakibara[25] to extract structures from a turbulent jet under the assumption of frozen turbulence, in which case the constraint (or event vector) was chosen such that the velocity vector is aligned with the direction that contributes greatest to the mean Reynolds shear stress. Staack *et al.*[28] chose their event vector to be a positive axial velocity fluctuation, with the resulting conditional velocity field roughly conforming to the characteristic "C-shape" associated with decaying vortex rings originating upstream. Ambiguity resulting from the under-constrained choice of event vector means that the resulting conditional structure is most likely the superposition of multiple real coherent flow structures of differing orientation.

In order to identify and investigate the dynamics of coherent structures and thus avoid ambiguity resulting from conditional sampling, the dynamic evolution of the whole flow field is of interest. Violato and Scarano[12] performed time-resolved TPIV measurements of coherent structure evolution relating to the instability of vortex rings in the near-field of turbulent jets, with both round and chevroned inlets at $Re = 5000$. Four 1 Mpx sensors were employed at a repeat rate of 1 kHz projecting into a measurement domain (for the round jet case) of diameter 30 mm and an axial extent of 50 mm which is centered approximately three diameters downstream of the outlet. Using a cylindrical light volume, 60 vectors were computed across the 30 mm diameter using 40^3 vox windows with 75% overlap from 600 reconstructed planes in the depth. The time resolved data allowed for analysis of the growth and evolution of azimuthal instabilites in the vortex rings and the formation of secondary streamwise vortices.

II. EXPERIMENTAL SETUP

A. Jet tank

Figure 1(a) shows a schematic of the experimental setup, showing the arrangement of the four high-speed video cameras and the scanning of the laser volume. The test section consists of a 450 mm wide and 500 mm deep octagonal acrylic tank. The jet is fed by a displacement pump into a constant-head tank and enters the test section through a bottom wall-mounted circular tube of inner diameter $D_j = 5$ mm. Before entering the tank, the flow passes through a $L = 50$ cm long circular steel pipe, giving $L/D = 100$ to assure a fully developed turbulent flow. The flow rate is adjusted by raising the overhead tank and setting the pump rotation rate.

TABLE I. Turbulent properties of the water jet at the three Reynolds numbers are presented including different scanning protocols and image acquisition rates. The "Image Δt" represents the time interval between image pairs used in the cross correlation step, while "Flow Δt" is the time step of the advancing velocity field.

Reynolds number	Scanning protocol	V_j (m/s)	V_c (m/s)	No. of Volumes	Kolmogorov scale η (mm)	Interrogation window (mm)	Final window (px)	Image Δt (ms)	Flow Δt (ms)	Time-series length (volumes)
2640	Triple-pulse	0.53	0.0632	5	0.27	3.30	48	7.7	57.7	210
5280	Fast-scan	1.06	0.138	5	0.16	3.30	48	3.9	3.9	524
10700	Double-pulse	2.15	0.280	9	0.095	3.30	48	2.2	22.2	174
10700	Double-pulse (magnified)	2.15	0.280	5	0.096	1.46	64	2.2	22.2	174

The working liquid is water, seeded with 20–50 μm diameter PMMA encapsulated Rhodamine B fluorescent particles (Microparticles GmbH, PMMA-RhB-FRAK-B1430) with specific density of 1.19. The Reynolds number of the jet is based on the mean inlet velocity V_j and pipe diameter D_j,

$$Re = \frac{\rho V_j D_j}{\mu}, \tag{2}$$

where ρ and μ are the density and dynamic viscosity of the liquid. Herein, we show results for three flow-rates with corresponding $Re = 2640$, 5280, and 10 700, with additional flow quantities listed in Table I. The Kolmogorov length scale is calculated from the relation

$$\eta = \left(\frac{\nu^3}{\epsilon}\right)^{1/4}, \tag{3}$$

where the kinematic viscosity, ν of water is 1.08×10^{-6} m^2/s and the dissipation of turbulent kinetic energy, ϵ, is estimated (following Friehe, Van Atta, and Gibson[30]) as

$$\epsilon = 48 \frac{V_c^3}{D_j} \left(\frac{D_j}{x - x_0}\right)^4, \tag{4}$$

where V_c is the centerline velocity at the midpoint of the domain, x is the streamwise coordinate originating at the inlet and x_o is the virtual origin of the jet.

B. Laser-scanning

We use a galvanometer (VM2000, GSI Lumonics) with a mirror to scan the illumination volume. Volume generating optics are situated just before this along the beam path. The large distance between the galvano-mirror and the flow tank (2.5 m) ensures that the light volume enters the tank essentially normally to its surface, with incident angle $\theta < \pm 2^\circ$. Each volume slice spans about 100 mm in the vertical and is between 17 and 25 mm wide, depending on how many volumes are scanned. The experimental domain is centered 50 jet diameters downstream in the self-similar region of the jet, in an effort to capture the complex turbulent coherent structure. At this location, the jet half-width is 23.5 mm as estimated using self-similar scaling. An adjustable horizontal aperture is inserted before the galvanometer to make the illumination intensity as even as possible across the width. We use a dual-cavity high-repetition-rate pulsed Nd:YLF 527 nm laser (LDY300PIV, Litron), which can supply 20 mJ/pulse at the maximum camera acquisition rate of 1279 Hz. For sufficient illumination intensity while using the smallest aperture of *f*/32, we pulse the two cavities simultaneously for each video frame.

Three basic scanning schemes were successfully applied, with protocol waveforms shown in Figs. 4(a)–4(d). These are what we refer to as *double-pulse*, where two pulses spaced by "Image Δt" (see Table I) are pulsed in each volume before the galvanometer moves the laser to the adjacent volume, *triple-pulse* where a third pulse is used, or *fast-scan* where all volumes are first pulsed once in sequence before the second set of laser pulses. In all cases each pulse is recorded on a separate video frame. The third image sample acquired in the *triple-pulse* protocol allows for the calculation

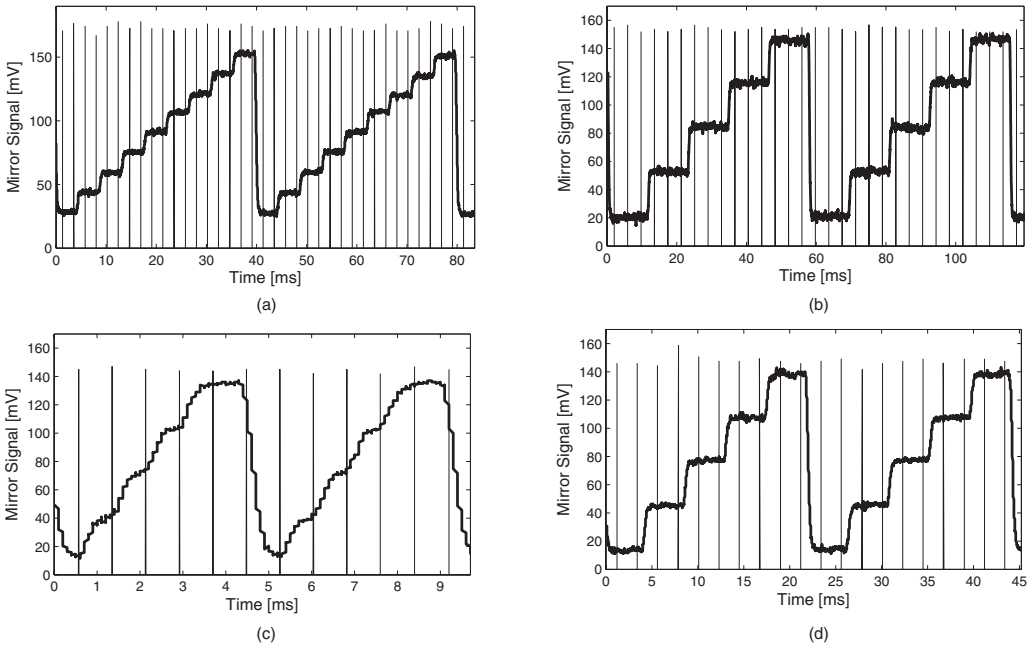

FIG. 4. The four different mirror scanning profiles used in the experiments, sampled using a Tektronix DPO 7254 Digital Oscilloscope, (a) 9 plane *double-pulse*, (b) 5 plane *triple-pulse*, (c) 5 plane *fast-scan* and (d) 5 plane *double-pulse*. The vertical axes correspond to the amplitudes of scanning signals inputted to the galvano-mirror. The 5V trigger signals of the pulsed-laser (seen here as impulse trains) are rescaled to fit the axes and superimposed to highlight the coordination between the mirror location and the image acquisition during scanning.

of the acceleration field across the entire domain. The acquisition speed is limited by two main factors: first, the maximum frame-rate of the high-speed cameras, while retaining maximum number of effective pixels on the CMOS sensor. Second, the maximum scanning rate of the galvanometer while shifting from the last volume back to the first volume. It was also possible to scan the light sheet and acquire images on both forward and backward passes but this was not pursued as it results in a non-uniform "Flow Δt" (see Table I) across the domain.

We use a commercial LaVision tomographic PIV system, with four 2016 × 2016 px CMOS high-speed video cameras (Dimax, PCO), which are capable of up to 1279 fps at full-frame resolution. Each camera can acquire 3150 images into built-in memory which determines the length of time series we can acquire for each experimental run. The cameras were arranged symmetrically facing the laser illumination, as shown in Fig. 1(a). They were angled at $\alpha = 45^\circ$ horizontally and $\beta = 30^\circ$ to the vertical, with water-filled prisms to minimize astigmatic aberrations. The cameras were mounted on a sturdy X-95 frame, which stood independently of the jet tank on the floor (Fig. 1(b)). The jet tank was rigidly connected to a large optical table supporting the laser scanning optics. We use identical lenses, mounted with Scheimpflug setups to retain acceptable focus over the entire 100 mm-wide volume, with an aperture of *f*/32. Imaging with *f*/22 was also successful, even though some edge particles were somewhat defocused. The data presented herein were acquired using the *f*/32 setting.

C. Calibration

Calibration was performed using a total of 11 planes over a 90 mm depth with a 3D translating calibration plate (Type 22, LaVision), containing on each side a dual-plane array of 3.2 mm bright white dots on a black background to deliver good contrast in the calibration images. The dots are spaced horizontally and vertically by 15 mm. This gives a total of 22 planes for each camera, spanning about 90% of the imaging domain, requiring very little extrapolation into the edges of the experimental volume. The calibration uses 3rd order polynomial mapping functions in *x*- and

y-directions, with linear interpolation in the z-direction. Volume self-calibration,[31] based on the reconstruction of bright particles within the illuminated particle fields in the actual experimental images, was performed using up to 20 planes for each volume. Disparity vectors of the order of 2-3 px were identified for each camera. Subsequent correction of the calibration polynomial coefficients reduced these disparities to the order of 0.1–0.2 pixels.

D. Tomographic reconstruction and vector calculation

The total reconstructed volume is about 100 mm cubed, but due to the optical arrangement, an ellipsoidal subsection delivers admissible vectors from the correlation step. The total volume consists of either 5 or 9 separately illuminated subvolumes, each of which is 25 or 17 mm wide, respectively, depending on the scanning protocol employed. A certain amount of laser overlap was used ($\simeq$ 3–4 mm) to ensure continuous data.

The raw images are first pre-processed in order to homogenize the particle intensities and to remove large-scale inhomogeneities in the image background. The local minimum intensity is subtracted from each pixel over a distance of 30 $\times$ 30 pixels. Pixel intensities are then normalized using the local average over a 300 $\times$ 300 pixel extent.

The particle intensities are reconstructed in a discretized 3D volume using five iterations of the MART algorithm[1] with a pixel-to-voxel-ratio of unity, where the intensity distribution is initialized using a multiplicative line of sight[3] estimate. This initialization ensures that regions outside the overlapping projection areas of all four cameras are excluded from the reconstruction.

These sub-volumes of the full experimental domain are reconstructed individually, where each volume uses its own individual self-calibration computed with only the particle images corresponding to that sub-volume.

The quality of the reconstruction can be quantified by estimating the intensity of the real reconstructed particles relative to the ghost particles within the volume. To estimate this, a region larger than the light sheet is reconstructed and the average intensity outside the light volume is compared to that inside (the reconstructed intensity outside being representative of the ghost intensity inside). Figure 5 shows the intensity profile of a reconstructed scanning volume averaged over an ensemble of reconstruction images. The light volume is approximately 17 mm thick which corresponds to about 250 vox for the 9-plane scanning protocol employed in this example. The

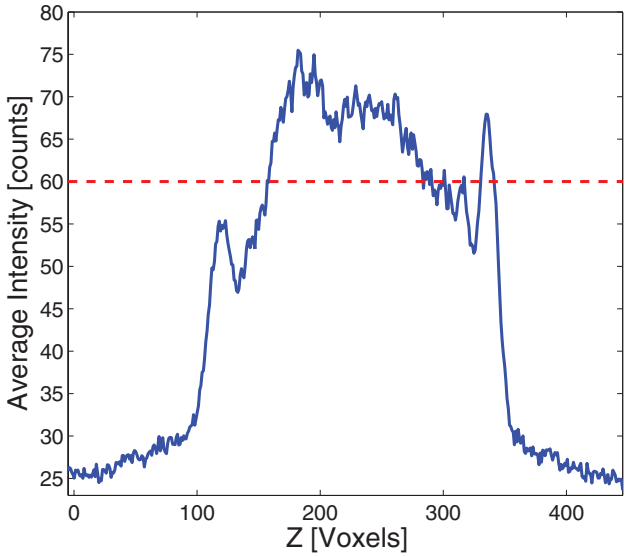

FIG. 5. Average reconstructed particle intensity across a scanning volume. The intensity of reconstructed particles outside the light sheet is about 50% of the level inside the sheet (the average level inside is shown with a red line), indicating a signal-to-noise ratio of about 2.

particles within the sheet have an intensity about 2 times greater than the ghosts. This signal-to-noise ratio is excellent considering that it is impossible to sharply cut off the edges of the beam prior to entering the experiment as is usually done in TPIV since we are scanning this light volume over a large spatial extent.

The 3D reconstructed particle volumes are then assembled to generate a single composite volume, where due to the illumination overlap employed between adjacent volumes, the regions of highest signal-to-noise ratio in each reconstructed scanning volume can be used in the assembly. This composite volume reconstruction contains approximately 1500 depthwise planes and approximately 4.4×10^9 voxels. The fraction of this 3D reconstructed image corresponding to overlap between all four cameras populates approximately 40% of this image, delivering a 3D distribution of particles within an approximately ellipsoidal region of 1.8×10^9 voxels. The volumes are analyzed to extract the velocity fields using a multi-pass cross-correlation procedure, with an initial window size of $64 \times 64 \times 64$ vox with 50% overlap and a final window size of $48 \times 48 \times 48$ vox with 75% overlap. This window size and overlap delivers 125 vectors in the depth direction.

Image deformation is applied to each correlation window[32] whilst outlier detection and recursive replacement by the average of admissible neighbor vectors over a $3 \times 3 \times 3$ vector region is performed after each correlation pass.[33]

The resulting vector field contains approximately 1×10^6 vectors in an ellipsoidal region at an equal spacing of 0.825 mm. We found this approach of assembling a composite reconstructed particle volume to give superior results compared to simply assembling the velocity results from each volume, owing to problems with edge distortions inherent in the multi-pass image deformation. The resulting velocity data contains about 96% good vectors. Smaller interrogation volumes were also investigated (see Sec. IV A), with the smallest windows size employed (32^3 vox) delivering over 3×10^6 vectors.

Each 3D-3C velocity field obtained from the correlation step, is smoothed by convolution with a Gaussian smoothing filter of standard deviation 0.65 (grid spacings) in order to remove high frequency noise. The size of the convolution kernel was chosen to match the dimension of the 3D correlation window employed in the final correlation pass so as to minimize loss of resolution. This corresponds to 2 grid points in all directions about each data point when 75% overlap is used. Spatial gradients are calculated using second-order central finite differences. The spectral resolution of finite-difference schemes are well documented[34] and the central difference scheme can be thought of as introducing a low-pass filtering operation to the gradient data whilst the largest scales should be captured well.

E. Assessment of data quality

The accuracy of velocity measurements obtained by Tomo-PIV has been the subject of recent comprehensive study by Atkinson *et al.*,[4] using both direct numerical simulations and experimental measurements in a turbulent boundary layer. They find a velocity uncertainty of about 0.3 px for the filtered velocity fields.

Our velocity uncertainty will arise from random as well as bias errors. The main source of random error is the subpixel error of the particle displacement, found by Gaussian interpolation of the correlation peak. For our 48^3 px correlation windows we typically have around 14 particles, making the error of the order of 0.1–0.2 px.[35] This random error translates into a random velocity error of 3.52 mm/s, or ~2.6% of the centerline velocity of 0.138 m/s.

This error affects directly the evaluation of the vorticity. Here vorticity was calculated using a second order central difference with a stencil spanning 2 velocity grid spacings. Following Fouras and Soria,[36] random error of the vorticity is derived by

$$\sigma_{\omega_z} = \frac{\sigma_u}{\delta},$$

where σ_u is the random error of the velocity and δ is the velocity sampling separation (the grid spacing). The actual vorticity of the coherent structure we captured in our measurement is estimated to be $\Omega \sim V/L$, where V is centerline velocity and L is the length scale of the coherent structures

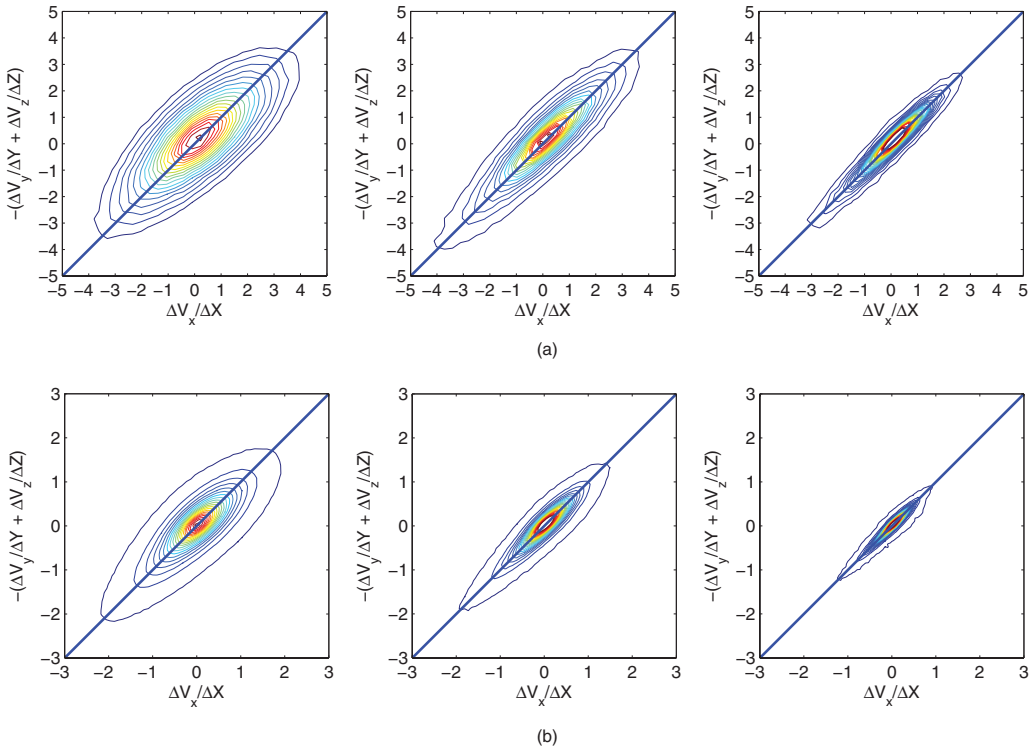

FIG. 6. Contours of the joint PDFs of select components of $\nabla \cdot \mathbf{V}$ for cube sizes (left to right) of W, 2W, and 4W. (a) Data correspond to the $Re = 10\,700$ case with 20 contour levels ranging from (left to right) 0.01–0.07, 0.01–0.2, and 0.01–0.6, respectively. (b) Data correspond to the $Re = 2,640$ case with 20 contour levels ranging from (left to right) 0.01–1, 0.01–2, and 0.01–7, respectively. Divergence free data lie along the 45° line. The distributions are highly peaked at the origin. ΔX, ΔY, and ΔZ represent the dimensions of the cubes used to generate each ensemble, while V_x, V_y, and V_z are the velocities averaged on the cube surfaces.

$\sim 4\delta$ for the approximate diameter of a structure. Thus the random error of the vorticity relative to the absolute value is estimated by

$$\frac{\sigma_{\omega_z}}{\Omega} = \frac{\sigma_u}{V}\frac{L}{\delta} = 4 \times 2.6\% \simeq 10\%.$$

The quality of the velocity field, and in particular the accuracy of the velocity gradients, can also be assessed by evaluating the residual of the continuity equation. Since the water flow in question is incompressible, dilatation effects are negligible and a solenoidal kinematic condition of $\nabla \cdot \mathbf{V} = 0$ should hold everywhere in the domain. Ensemble statistics of the velocity gradients were calculated using 870 random samples of data for $Re = 10\,700$ and again for 2100 samples of $Re = 2640$ where in the latter case the smallest resolved flow scale is obviously closer to η than in the former, since the absolute spatial resolution of both experiments is the same. Following the approach used by Zhang *et al.*[6] for the analysis of 3D-3C flow data, the velocity field is averaged and differenced over the surfaces of cubes of respective dimensions W, 2W, and 4W, where W is the window dimension employed in calculating the velocities by cross correlation and corresponds to the smallest length scale resolved in the experiment. Figures 6(a) and 6(b) corresponding to $Re = 10\,700$ and $Re = 2640$, respectively, show joint PDFs of $\frac{\Delta V_x}{\Delta X}$ and $-(\frac{\Delta V_y}{\Delta Y} + \frac{\Delta V_z}{\Delta Z})$ calculated for cubes of dimension W, 2W and 4W. Divergence free data lies along a 45° line. For the $Re = 10\,700$ data, the correlation coefficients between the two parameters are 0.73, 0.89, and 0.96 for cubes of W, 2W, and 4W, respectively. For the $Re = 2640$ case, the corresponding correlation coefficients are 0.79, 0.91, and 0.96. Both results for cube dimension W, which matches the spatial resolution of the experiment, compare reasonably well to the value of 0.82 determined by Ganapathisubramani

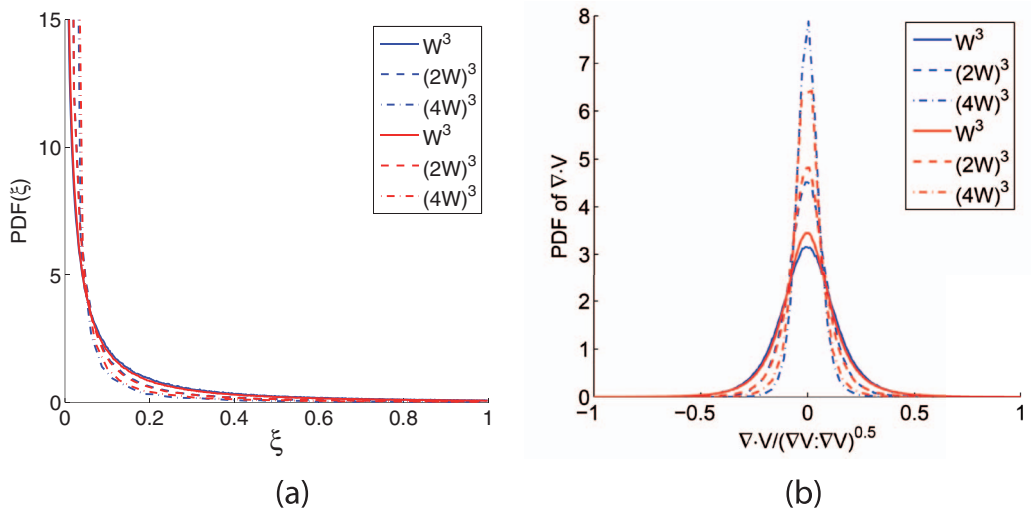

FIG. 7. (a) PDF of divergence error, ξ, as proposed by Zhang *et al.*[6] (data curves are highly overlapping) (b) PDF of $\nabla \cdot \mathbf{V}$ normalized by the 2-norm of the velocity gradient tensor. Blue and red lines correspond to the $Re = 10\,700$ and $Re = 2640$ cases, respectively.

et al.[26] who measured the velocity gradients in a turbulent co-flowing jet using stereoscopic PIV invoking a frozen turbulence assumption.

Zhang, Tao, and Katz[6] presented the PDF of a parameter

$$\xi = \frac{(\nabla \cdot \mathbf{V})^2}{tr\,(\nabla \mathbf{V} \cdot \nabla \mathbf{V})} \tag{5}$$

encapsulating the deviation of their data from the solenoidal condition. The value of this parameter lies between 0 and 1, with 0 indicating a solenoidal field and 1 indicating that the gradients are completely independent. Figure 7(a) shows PDFs of ξ for cube dimensions of W, 2W, and 4W with corresponding means of 0.36, 0.19, and 0.09 for $Re = 10\,700$ and 0.33, 0.18, and 0.11, respectively, for the $Re = 2640$ case. These values are in reasonable agreement with the corresponding mean values of 0.5, 0.20, and 0.075 determined by Zhang *et al.*[6] for their experiments in channel flow using holographic PIV.

The divergence error may also be quantified by examining its PDF. Figure 7(b) shows PDFs of $\nabla \cdot \mathbf{V}$ normalized by the 2-norm of the velocity gradient tensor $(\nabla \mathbf{V} : \nabla \mathbf{V})^{0.5}$ calculated for cube sizes of W, 2W, and 4W for both the $Re = 10\,700$ and $Re = 2640$ cases. The distributions all appear to be Gaussian with zero mean. The RMS of these distributions for cube sizes of W, 2W, and 4W are 0.15, 0.11, and 0.06, respectively, for the $Re = 10\,700$ case and 0.15, 0.11, and 0.07 for the $Re = 2640$ case. This statistic was also calculated using central differences and the RMS for both cases was found to be 0.40. This is in reasonable agreement with the value of 0.35 reported by Khashehchi *et al.*[11] in their TPIV analysis of a turbulent round jet. In dual-plane stereo-PIV (DSPIV) experiments performed in the far-field region of a co-flowing turbulent jet, where a spatial resolution of 5η was achieved, Mullin and Dahm[27] performed this same analysis using central differences for the calculation of spatial gradients and also determined the RMS of the distribution to be 0.35. The value of 0.25 reported by Ganapathisubramani *et al.*[26] (who also used central differences in their analyses) is much lower, where a spatial resolution of 3η is achieved by their planar technique.

In order to quantify the importance of the relative divergence error, one should compare it to the magnitude of the other velocity gradients in the flow. Figures 8(a) and 8(b) show contours of the joints PDFs of the 2-norm of the velocity gradient tensor and the divergence error $(\nabla \cdot \mathbf{V})$. The divergence error is normalized by the 2-norm of the velocity gradient tensor, where again the gradients are approximated by averaging the velocity components over cubes of size W, 2W, and 4W.

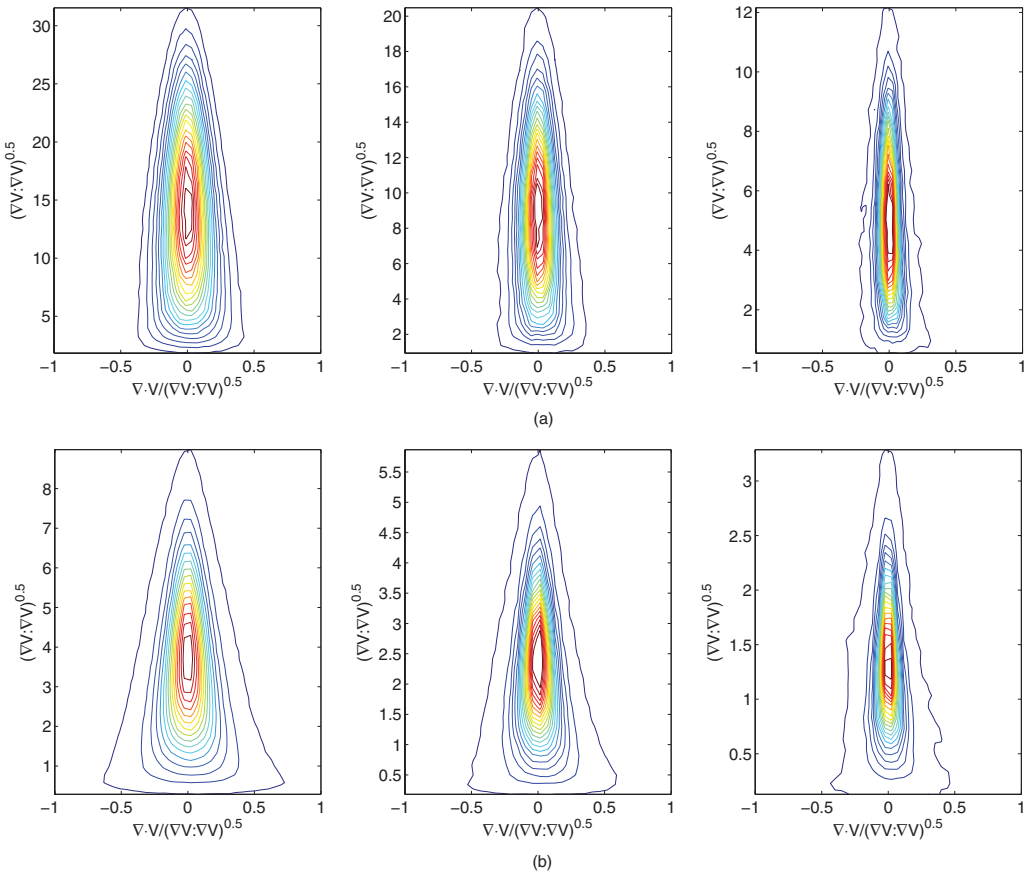

FIG. 8. Contours of the joint PDF of the 2-norm of the velocity gradient tensor and the normalized divergence residual for cube sizes (left to right) of W, 2W, and 4W. (a) Data correspond to the $Re = 10\,700$ case with 20 contour levels ranging from (left to right) 0.01–0.2, 0.01–0.6, and 0.01-1.2, respectively, and (b) data correspond to the $Re = 2640$ case with 20 contour levels ranging from (left to right) 0.01–1, 0.01–1.7, and 0.01–5, respectively.

The distributions appear to be symmetric about the line $\nabla \cdot \mathbf{V} = 0$, with the highest values of relative divergence error occurring for lower magnitudes of the velocity gradients. This result leads us to conclude that the more intense gradients, and thus the regions of intense vorticity which are of interest in this investigation, should exhibit the lowest divergence error and should be captured more accurately. This conclusion is in agreement with the results of Ganapathisubramani *et al.*[26] and Mullin and Dahm.[27]

Error can also be introduced into the velocity measurements at the correlation step due to the phenomenon known as "peak-locking," where the displacements calculated in the correlation are biased towards integer voxel values. The presence of peak-locking can be investigated by examining PDFs of the velocity components in voxel space. To estimate bias in the data, modulo operation with divisor 0.5 voxel is applied to each velocity component at every point. This approach maps velocities with a sub-voxel component greater than 0.5 vox onto the interval 0–0.5 vox. For a velocity field that exhibits no peak-locking, this ensemble should have a mean close to 0.25 vox which essentially indicates that the data is equally likely to lie close to a half-voxel displacement as to an integer value. A mean close to zero would indicate strong bias toward integer values. For a sample of our data, PDFs were generated for each velocity component where the means were all found to be in the range 0.244–0.256 vox indicating essentially no peak-locking effect.

One must also consider other possible sources of bias errors in the velocity measurements.[4,37] Having volume data eliminates one well known source of bias error present for 2D PIV, i.e., when the fastest moving particles can leave the laser sheet.[35]

Bias can result from numerous other effects[13] such as: particle loss and uneven illumination due to laser sheet non-uniformity, sheet misalignment between pulses, and irregular particle shape and size; any inhomogeneity in the particle distribution; persistent non-random noise due to camera hot-pixels and light diffusion due to multiple scattering effects. The transmission of these errors into our measurements was minimized as much as possible in three ways: by sharply cutting the beam profile at the edges to avoid the Gaussian decay of beam intensity. By using a very low aperture setting to ensure that all particles were in good focus, but having more than 2 pixels in diameter of the airy disk and by using fluorescent particles in order to avoid scattering effects.

Bias errors can also arise owing to distortions due to viewing windows and optics, which we have here minimized with the water-filled prisms and Scheimpflug adapters. One indication of these optical distortions are the errors in the volume self-calibration applied to the raw image data, which in the present study resulted in a final disparity of 0.1–0.2 px. These optical distortions are expected to vary slowly in space and therefore we expect the disparity particle positions to be an upper bound for the bias.

Bias is introduced into the calculation of velocity gradients as mentioned in Soria,[37] where it is noted that low order finite differencing biases derivatives to the lower regions of the wavenumber spectrum. In Sec. II D we refer to the spectral resolution of FD schemes and the analysis of Lele[34] and the low pass filtering property of the central differences employed in our work.

Atkinson *et al.*[4] show that in the boundary layer ghost particles can cause bias in the region near the wall which has large mean velocity gradient. The ghost particles cause a bias which tends to reduce this velocity gradient.[16] However, for our jet flow the mean velocity gradients are much weaker than in the near-wall region of the boundary layer and we do not expect significant bias of this type. We also use image deformation during the multi-step correlations, which has been shown to reduce such bias.[4]

The experimental domains in the data presented thus far were designed to capture the entire extent of the jet (up to 2.25 half-widths in all directions about the centerline) with the velocity field resolved to within 10–30 Kolmogorov scales η in terms of the interrogation window size, depending on the Reynolds number used. This lack of full spatial resolution will inevitably affect the calculation of spatial derivative quantities and bias the magnitude of the vorticity to lower values.[4,37,38] In order to estimate the effect of spatial resolution on the vorticity, we repeated the $Re = 10\,700$ experiments under identical conditions while using a factor of 2.25 higher optical magnification to achieve higher spatial sampling. Using this higher level of magnification means only a sub-region of the jet width is captured. The PDF of vorticity magnitude in Fig. 9 clearly shows that improving the spatial resolution to 15η from 30η shifts the vorticity PDF to higher values by resolving finer scales of the spatial gradients, while both reconstructions should capture the large coherent vortical structures.

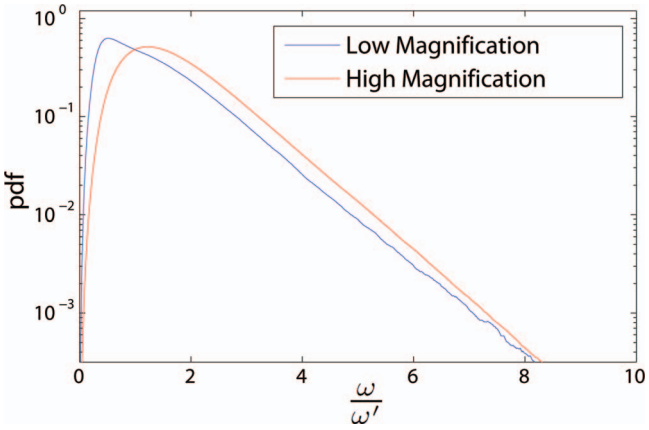

FIG. 9. Vorticity magnitude PDFs scaled by the RMS vorticity, $\omega\prime$, for $Re = 10700$ experiments using different optical magnifications. The statistical ensembles for both PDFs were extracted from the same subsections of the jet, between 1 and 1.5 half-widths (r_{half}).

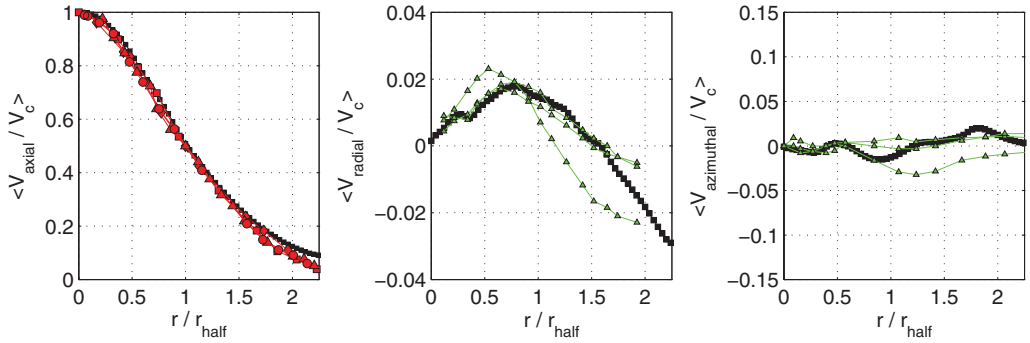

FIG. 10. (Left to right) Mean axial, radial, and azimuthal velocity profiles for $Re = 10\,700$. Black data points are our scanning TPIV results while red and green data points correspond to hot-wire[23] and stereo-PIV[25] data, respectively.

However, recent experiments of Tokgoz *et al.*[39] show that even though the primary spatial resolution must be based on the interrogation window size, overlapping of the adjacent windows extracts some of the finer-resolution gradient information, despite giving highly dependent velocity samples. This they demonstrate by measuring the dissipation rate of turbulent flow in a Taylor-Couette device, where torque-measurements provide an independent estimate of the dissipation. Using 75% overlap of interrogation windows, they captured more of the dissipation, demonstrating that some of the gradient information is better captured than for none or 50% overlap. We expect the same to be true in the present study.

III. FLOW STATISTICS

A. Mean and RMS velocity statistics

First and second order velocity statistics were calculated in order to qualify the canonical nature of the jet flow field. Radial profiles of mean velocity components are shown in Fig. 10 where the radial coordinates are normalized by the jet half-width, r_{half}. Figures 11(a) and 11(b) show that the jet is statistically axisymmetric across the multiple scanning volumes exhibiting an almost perfectly circular axial mean profile when viewed along the flow axis.

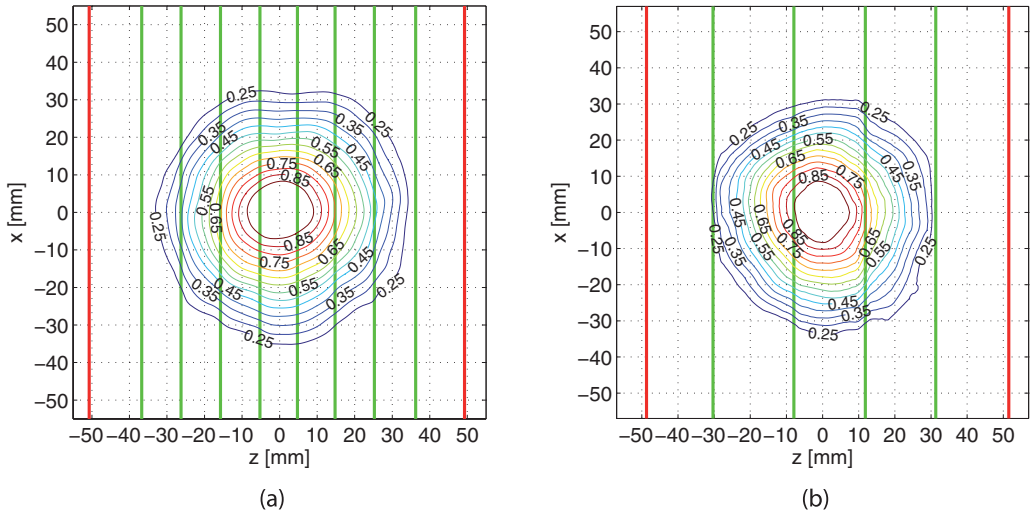

FIG. 11. (a) Axial mean contours for $Re = 10\,700$ where 9 scanning volumes were employed. (b) Axial mean contours for $Re = 2640$ where 5 scanning volumes were employed. Green lines represent the interfaces between the assembled reconstructed particle images and red lines represent the extents of the reconstructed domains for both cases.

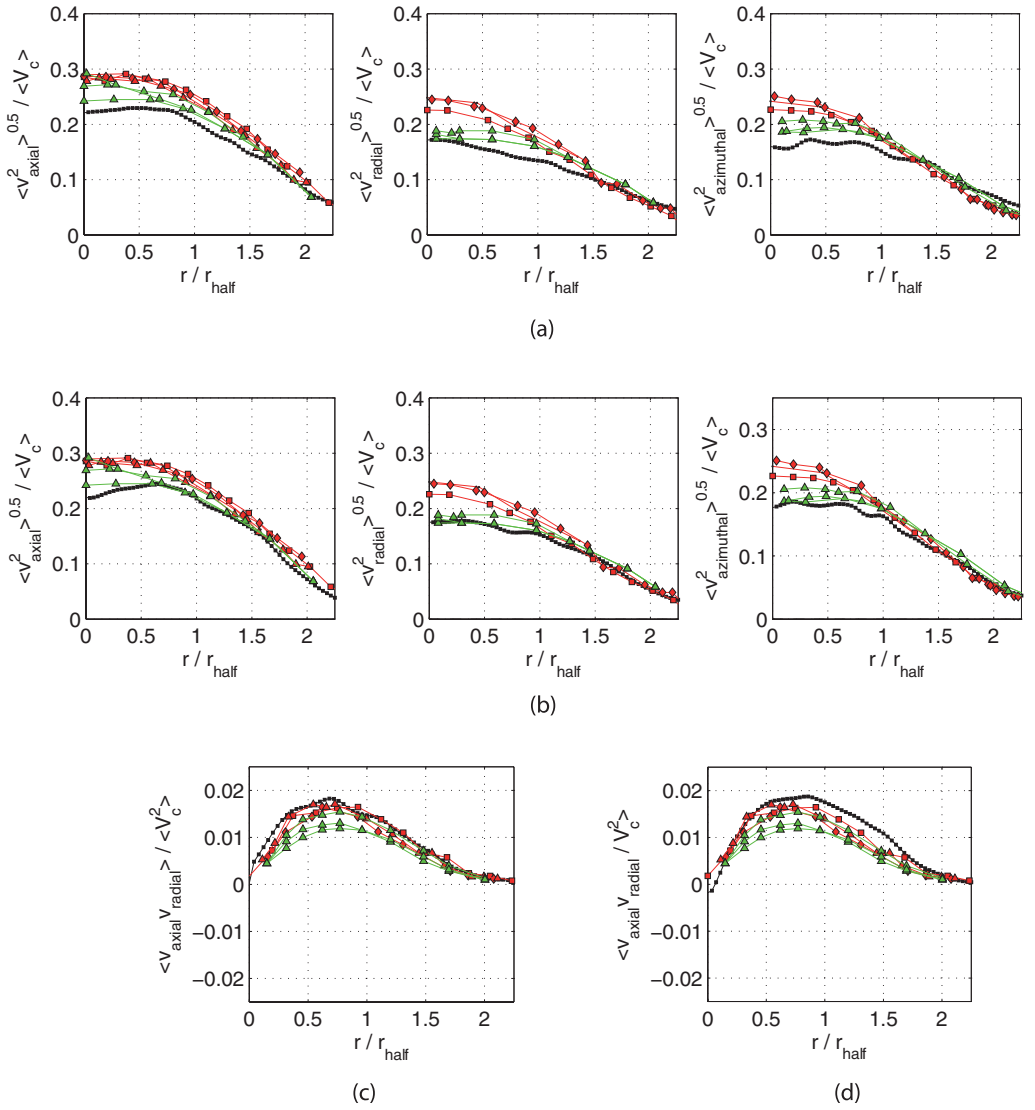

FIG. 12. (a) (Left to right) axial, radial and azimuthal RMS profiles for $Re = 10\,700$, (b) (left to right) axial, radial, and azimuthal RMS profiles for $Re = 2640$. One component of the Reynolds stress tensor for (c) $Re = 10\,700$ and (d) $Re = 2640$. Black data points are scanning-TPIV results while red and green data points correspond to hot-wire[23] and stereo-PIV[25] data, respectively.

These statistics were calculated from 870 volume samples from experiments with $Re = 10\,700$. The data agree quite well with other measurements of the turbulent round jet.[23,25] The root-mean-squared (RMS) velocity data for $Re = 10\,700$ (Fig. 12(a)) and for $Re = 2640$ (Fig. 12(b)) are also in reasonable agreement with the existing data. However, both the stereo-PIV and scanning-TPIV techniques underestimate the magnitude of the RMS profiles when compared to the classical hot-wire data. This can be attributed to the limited spatial resolution of these PIV techniques which do not cover the whole range of wave numbers in the energy spectrum and also to the smoothing performed on the raw vector data, which may decrease the intensity of the velocity fluctuations. A profile of one component of the Reynolds stress tensor for $Re = 10\,700$ (Fig. 12(c)) and $Re = 2640$ (Fig. 12(d)) seem to agree well with existing data.

As an example of the power of the scanning technique, we demonstrate the effect of the presence of ghost particles on the fidelity of velocity measurements in our 100 mm depth experimental domain. Data for a 9 volume scanning experiment is considered and the scanning technique is compared to

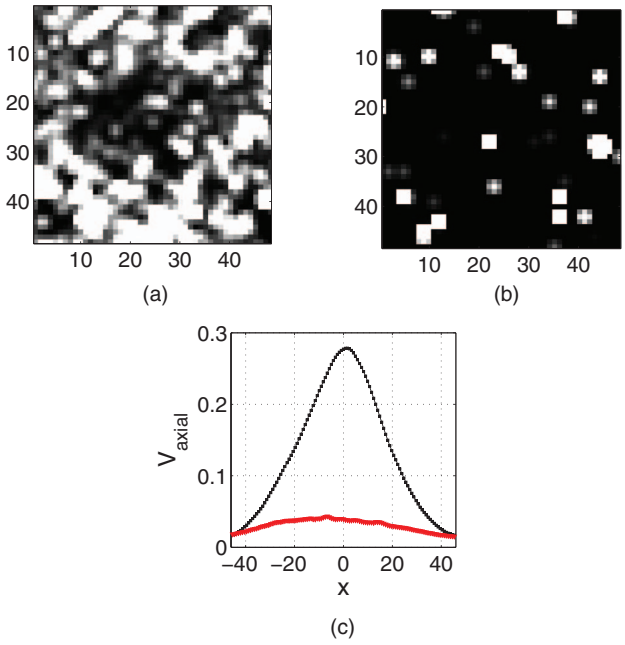

FIG. 13. (a) 2D projection of a 48^3 vox region of the reconstructed particle image for the full illuminated domain (see Fig. 2(b)), (b) 2D projection of the same 48^3 vox region using a scanning protocol, (c) comparison of mean axial velocity profiles across the jet for the fully illuminated (red) and scanning (black) cases highlighting the failure of full volume illumination.

the alternative, i.e., full volume illumination, where the entire 100 mm depth is illuminated at once. In order to simulate this, the particle images corresponding to all 9 volumes in a scanning pass were superposed for each camera to represent the particle image density (*ppp*) that would be measured on the sensors (see Fig. 2). The images are essentially saturated and the image density far exceeds the optimal value of 0.05.

These images were reconstructed in 3D using the accurate calibrations computed using the scanning data to approximate the ideal case, as any self-calibration that was attempted using the superposed images was unsuccessful. Figures 13(a) and 13(b) show a comparison of the MART reconstruction results for the full-volume illumination simulation and the scanning experiment, respectively, over the same 48^3 vox region which is exactly one correlation window size for our data. The reconstruction corresponding to the scanning case contains about 20 particles while the full volume case is almost completed full of reconstructed light and it is difficult to identify individual particles. While it is not immediately clear that the increased particle density in Fig. 13(a) corresponds to a high population of ghost particles, by comparing the velocity fields resulting from correlation of each of the two data sets the impact is obvious. Figure 13(c) shows a comparison of the mean axial velocities calculated using both reconstructions.

While the scanning case shows the expected bell-curve shape and exhibits a centerline velocity that agrees with what should be expected based on the self-similar scaling of the axial velocity with downstream coordinate, the full volume case is massively attenuated and matches the bell-curve profile only at the very edges of the jet. The implications of increased seeding density are severe for the full illumination case where ghost particles in the center of the jet are formed from pairs from a set of slow moving real particles on the jet periphery. Since coherent ghost particles (i.e., ghost particles that are present in both images in the correlation) are generally displaced by the average of the particles that form them[16] the correlation will be heavily biased towards the velocity of the slow moving peripheral particles. The effect on spatial gradients is also severe as the slow moving ghosts smooth out all the fine-scale information.

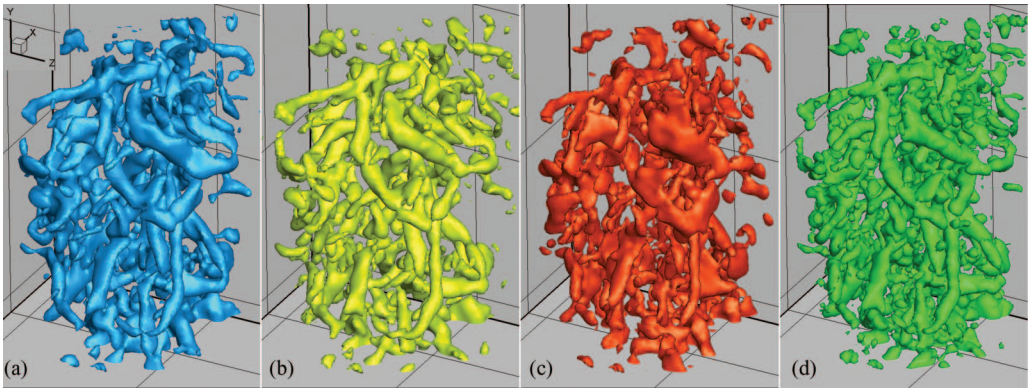

FIG. 14. Instantaneous iso-surfaces of coherent structures, identified using four different methods, of (a) vorticity magnitude, $\omega = 11\ s^{-1}$, (b) $\Delta = 20\ s^{-3/2}$, (c) $\lambda_2 = -28\ s^{-2}$, and (d) $Q = 800\ s^{-2}$. Data correspond to $Re = 2640$.

IV. ANALYSIS OF COHERENT STRUCTURES

Since the aim of our experimental approach is to better capture the time-evolving coherent structures in a canonical turbulent flow, it is appropriate at this point to establish some criteria for identifying the motions that we expect to resolve. While an objective definition of a fluid vortex is still elusive, we can still postulate certain characteristics of the dynamic coherence that we expect to exist in our data. For laminar inlet conditions, the prominent flow feature in the region close to the nozzle of a round jet is the roll-up of the vortex sheet into axisymmetric vortex rings due to Kelvin-Helmholtz instability.[12,40,41] Azimuthal instability of the vortex rings lead to the formation of secondary streamwise vortices which distort the main rings further to the point of breakdown.[42] For our fully turbulent inlet conditions these vortex structures will not be as dominant as for a transitional flow but we do expect the flow features in our downstream experimental domain to be highly vortical.[7] Using vorticity as a first choice for a characterization criterion, the vorticity magnitude field is thresholded to isolate the most intensely vortical regions. Figure 14(a) shows iso-surfaces of this thresholded field for an instantaneous snapshot of flow, which appears to highlight a complex network of tube-like vortical structures oriented both axially and azimuthally. Purely radial structures are expected to be absent due to the lack of azimuthal mean shear.

A. Coherent structure extraction

Since structure extraction using a vorticity magnitude criterion suffers from the ambiguity between tube-like structures and vortex sheets, other point-based vortex identification criteria using the invariants of the velocity gradient tensor, have been proposed. Figure 14 compares our vorticity iso-surfaces to three popular such approaches, i.e., those of Δ (Chong *et al.*[43]), λ_2 (Jeong and Hussain[44]) and Q (Hunt *et al.*[45]) calculated for the same instantaneous velocity volume. These more complex methods are in overall agreement with the result for vorticity magnitude with some difference in the larger azimuthal structures noticed in the λ_2 case where the tubes take on a slightly more sheet-like appearance over their extent. The visualization of Q was also seen to contain a higher population of small intense blobs along with the tube-like structures. We conclude that thresholding the vorticity magnitude is an effective way of extracting the coherent structures in our flow.

Figure 15(a) shows the time evolution of these vortical structures with three snapshots of vorticity magnitude iso-surfaces for the $Re = 2640$ case, where the snapshots are separated by three flow time steps. The flow is dominated by an apparently random jumble of vortices of various orientation (see videos 1 and 2 with Fig. 15). Multiple azimuthally oriented "C-shaped" structures can also be seen to translate in the streamwise (vertical) direction. A collection of such structures is highlighted where one is seen to advect, decrease in diameter and break over this interval.

Figure 15(b) shows single instantaneous snapshots of the $Re = 5280$ (left) and $Re = 10\,700$ (right) experiments. These higher Reynolds number flows exhibit tube-like structures albeit of

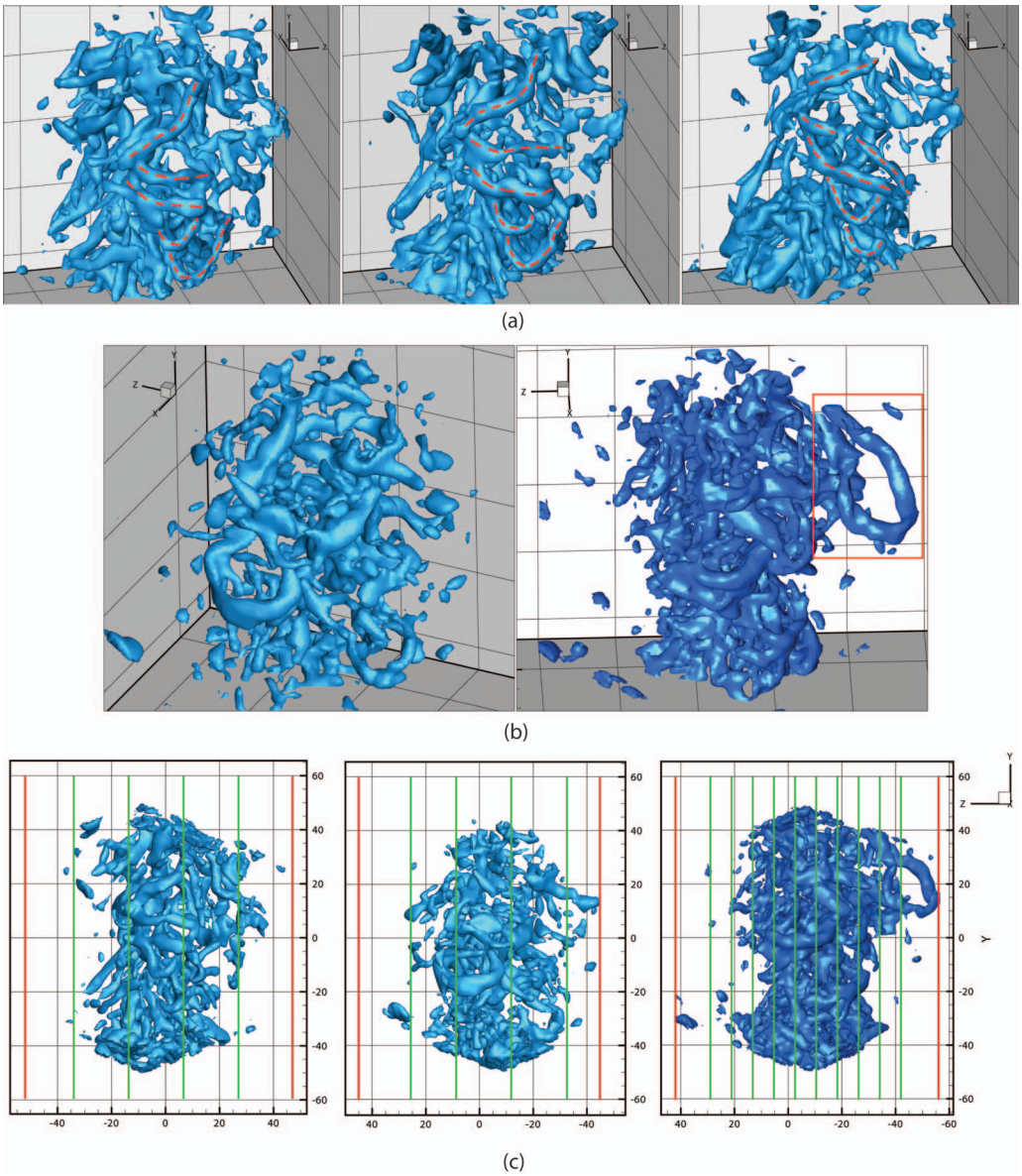

FIG. 15. (a) Three snapshots of $Re = 2640$ time-series data over a 0.35 s interval with vorticity magnitude iso-surfaces $\omega = 11\ \mathrm{s}^{-1}$. Each snapshot is separated by three time steps (0.17 s) to highlight the evolution of the loops. A collection of loops are highlighted with red dashed lines. (b) Vorticity magnitude iso-surfaces for $Re = 5280$ (left) and $Re = 10\,700$ (right) with values of $\omega = 21\ \mathrm{s}^{-1}$ and $35\ \mathrm{s}^{-1}$, respectively. A large intense hairpin loop is highlighted for the $Re = 10\,700$ case (red rectangle). (c) Vorticity magnitude iso-surfaces for (left to right) $Re = 2640$, $Re = 5280$ and $Re = 10\,700$ with iso-surface values of $\omega = 11$, 21, and $35\ \mathrm{s}^{-1}$, respectively. The views are orthogonal to the scanning direction for each case. The red lines in each image indicate the extent of the reconstructed domains, while the green lines indicate the intersection between adjacent reconstructed scanning volumes (enhanced online) [URL: http://dx.doi.org/10.1063/1.4790640.1] [URL: http://dx.doi.org/10.1063/1.4790640.2].

smaller scale than for the $Re = 2640$ case but the most intense motions are still captured well. Figure 15(c) highlights the continuity of the data across the scanning volumes, where individual loops can be seen spanning the interfaces between individual reconstructed scanning volumes. The interfacial planes are marked by vertical lines.

As a simple example of the spatio-temporal sampling achieved for the $Re = 10700$ case, eight consecutive snapshots of the hairpin-loop structure highlighted in Fig. 15(b) are presented in

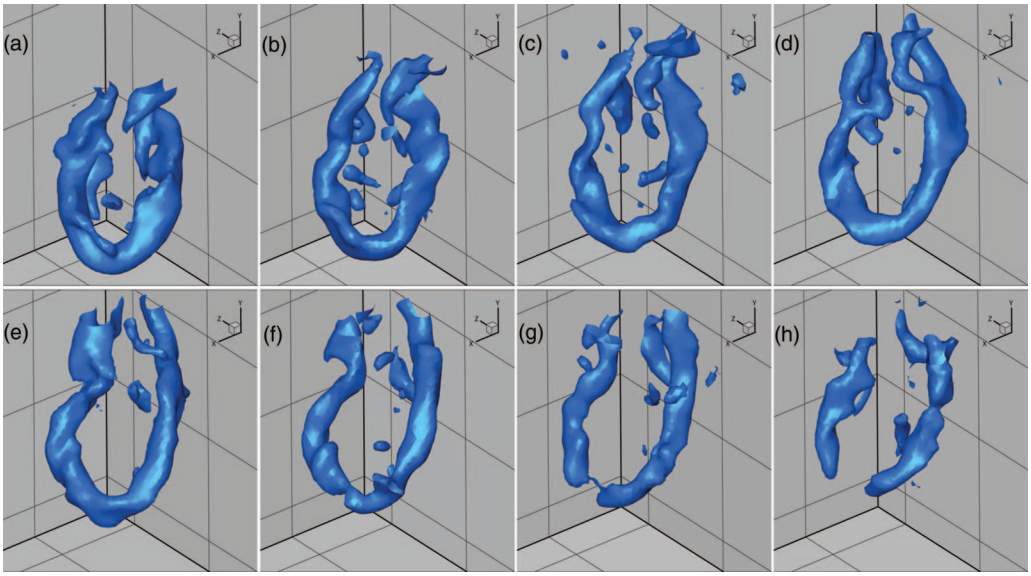

FIG. 16. (a)-(h) Evolution of a single "C-shaped" structure for the $Re = 10700$ case over a 0.15 s interval, with 0.022 s between subsequent snapshots.

Figs. 16(a)–16(h). This loop has been "ejected" into the outer irrotational region of the jet with the loop head located at approximately $r/r_{half} = 2$ in the presented sequence, where r_{half} is approximately 24 mm at this downstream location. This structure is similar in spatial coherence to the "vortex strings" identified by Matsuda and Sakakibara[25] in their analysis of the vortical structure of a turbulent jet. In their data, the location of the center of curvature of the hair-pin loop which was identified from both instantaneous vorticity iso-surfaces and linear stochastic estimation, was $r/r_{half} = 1.5$. This is close to our present observation and coincides with an earlier stage of the ejection of the loop from the jet core into the quiescent region.

In the first frame, Fig. 16(a), the loop appears to have a smooth surface curvature apart from some disturbances at the ends of both hairpin legs. In the second frame (b), the disturbance in the left leg appears to have grown into a significant oscillation visible along most of the left leg. This oscillation persists in the next 2 frames (c),(d) and by frames (e) and (f) has developed a significant curvature while the head of the loop breaks down as evidenced by the decreased head diameter. This indicates a decrease in local vorticity magnitude as a constant threshold value is employed throughout the evolution. In frames (g) and (h) the vorticity in the loop head has diminished further and the loop breaks at two points. Since the head of the loop is quasi-parallel to the azimuthal direction, where the axial stretching is rather small compared to the leg extending in the radial streamwise direction, amplification of the vorticity is not expected. Rather than intensifying the vorticity, it breaks down due to viscous diffusion of its concentrated vorticity.

While the majority of the experimental data presented in this paper correspond to image correlation using 48^3 vox windows, the possibility of using smaller window sizes was also investigated. Figure 17 shows instantaneous iso-surface visualizations of $\omega = 11\ s^{-1}$ for the $Re = 2\,640$ case using different final correlation window sizes on the same reconstructed particle data. The smaller correlation windows capture the coherence of the large tube-like structures while also introducing noise in regions where data points corresponding to bad-vectors must be interpolated. For the smallest window size tested, 32^3 vox, the flow is resolved to about 8η indicating that the scanning technique can deliver a higher degree of fidelity across the entire jet width. The 36^3 and 32^3 vox cases deliver about 2.2×10^6 and 3×10^6 vectors, respectively, but require increased levels of smoothing and interpolation as the number of good vectors is about 90% and 80% for each case. The additional smoothing was accomplished by repeating 2–4 times the same Gaussian filtering, its

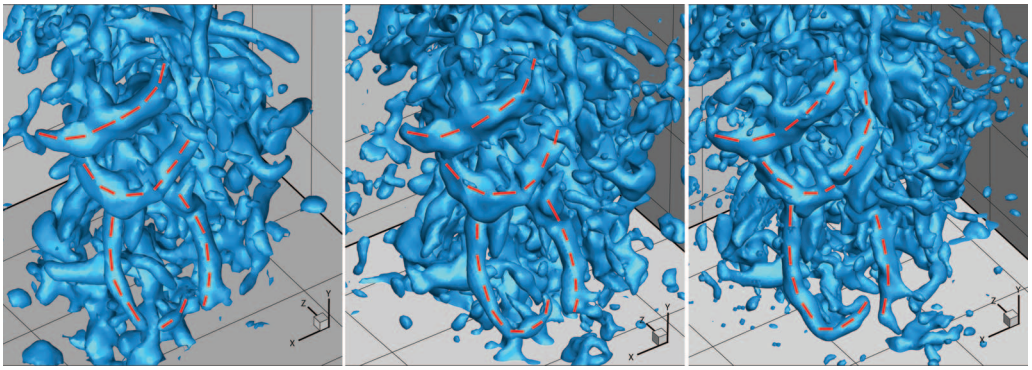

FIG. 17. Comparison of data quality for velocity calculation using different final correlation window sizes (left to right), 48^3, 36^3, and 32^3 voxels with 75% overlap in each case. These correlation window sizes deliver 1×10^6, 2.2×10^6, and 3×10^6 vectors, respectively. A few equivalent coherent structures are highlighted in red in each image.

size now matched to the smaller interrogation window. Data corresponding to 40^3 delivers about 1.6×10^6 vectors with 94% good vectors (data not shown).

The statistical velocity data presented previously and the coherent structure data presented herein were computed using 48^3 vox windows due to the large calculation times required for employing the smaller windows when reducing the long time-series of our experiments.

B. Turbulent transport

Other quantities of interest when considering the dynamics of coherent motions are their contribution to the kinetic energy of the turbulent fluctuations or transport. Production of turbulence kinetic energy in turbulent flows is usually high in regions where the local velocity is increased due to vortex induction, which correspond to regions of high Reynolds shear stress. Figure 18 shows the evolution (left to right) of positive and negative Reynolds shear stresses, $v_{axial}v_{radial}$, resulting from vortex induced motion away from and towards the jet axis, respectively (see video 3 with Fig. 18). The regions of both positive and negative Reynolds stress are spatially and temporally coherent, with intense positive stress occurring between the legs and close to the head of the vortex loops highlighted by the dashed lines. Positive Reynolds stress correspond to regions of positive turbulent production as they are aligned with the dominant mean gradient of the axial velocity in the jet. Figure 19 shows an instantaneous snapshot of production (blue) and dissipation (red). Production is found to be high in-between the legs and close to the heads of the vortex loops while dissipation is also high in these regions. This approximation of the dissipation is not expected to be highly representative of the most intense dissipation as this data set is only resolved to 12η, and thus does not capture the smallest dissipation length scales. For a full investigation of the behavior of dissipation, η should be fully resolved which requires the use of higher levels of optical magnification and, inevitably, lower Reynolds numbers in order to increase the absolute size of η. This need for high magnification unfortunately eliminates the possibility of resolving the large scale structure of the flow. Dissipation range resolution PIV experiments have been successfully performed by Worth and Nickels[46] using TPIV, and by Diez *et al.*[47] using scanning digital PIV. The production of turbulence kinetic energy is also conjectured to be strongly linked to the stretching of vortex lines and the associated generation of smaller vorticity length scales, as predicted by cascade theory. While production may be at its peak away from the core of the vortex, it may be also of interest to investigate the production associated with the stretching of these intense vortex lines close to the core. We show in Secs. IV C and IV D the capability to investigate the evolution of the production and dissipation signature close to the vortex loops using our time-resolved data.

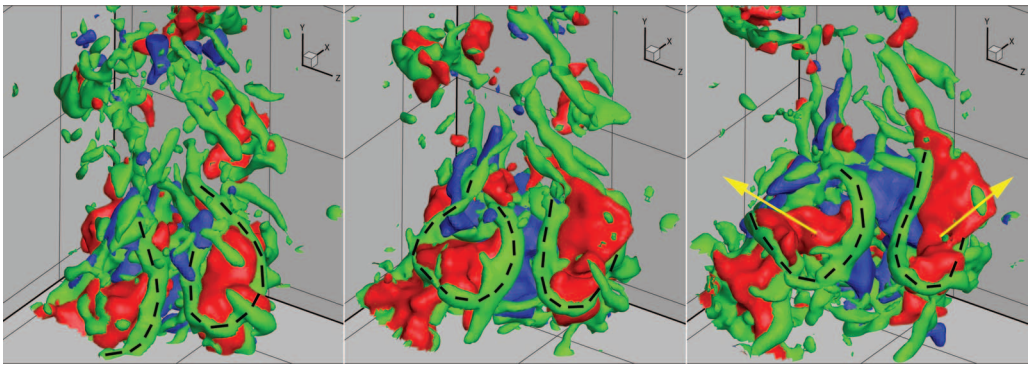

FIG. 18. Evolution of vortical loops (green vorticity isosurfaces with $\omega = 11\ \mathrm{s}^{-1}$) and instantaneous Reynolds stress $v_{axial}v_{radial}$ for $Re = 2640$. Each snapshot of the sequence is separated by 5 time steps (0.29 s) for a total interval of 0.58 s. A positive isosurface value of Reynolds stress is shown in red ($v_{axial}v_{radial} = 4 \times 10^{-5}\ \mathrm{m}^2/\mathrm{s}^2$) while the blue isosurfaces correspond to a negative value ($v_{axial}v_{radial} = -1.5 \times 10^{-5}\ \mathrm{m}^2/\mathrm{s}^2$). The yellow arrows in the final frame highlight the approximate direction of fluid flow resulting from intense vortex induction caused by the concentrated vorticity in the loops highlighted with dashed-lines (enhanced online) [URL: http://dx.doi.org/10.1063/1.4790640.3].

C. Coherent structure evolution

To highlight the quality of our time-resolved data sets it is of interest to extract time-resolved data pertaining to the evolution of the coherent structures. Rather than identifying structures visually as was performed in Secs. IV A and IV B, it is useful to implement an automatic procedure to identify individual structures and follow them over a sequence of time steps.

A simple structure identification process was implemented to identify particularly intense structures and follow their evolution over an interval of the time series, using a vorticity magnitude criterion. The data is thresholded based on some relatively large value of vorticity magnitude and an ensemble of structures in each frame are identified as simply connected 3D regions exceeding this threshold. To track structures in subsequent frames, the centroid of each structure is advected with the mean velocity within the structure. The advected centroid is then used as an initial guess for a search algorithm that compares candidate structures in the vicinity of this point to that structure in the previous frame. A comparison between the volumes of the structures was found to be a robust criterion for choosing from candidate structures as most are found to vary quite minimally in volume over the course of a time step due to the high degree of temporal sampling employed.

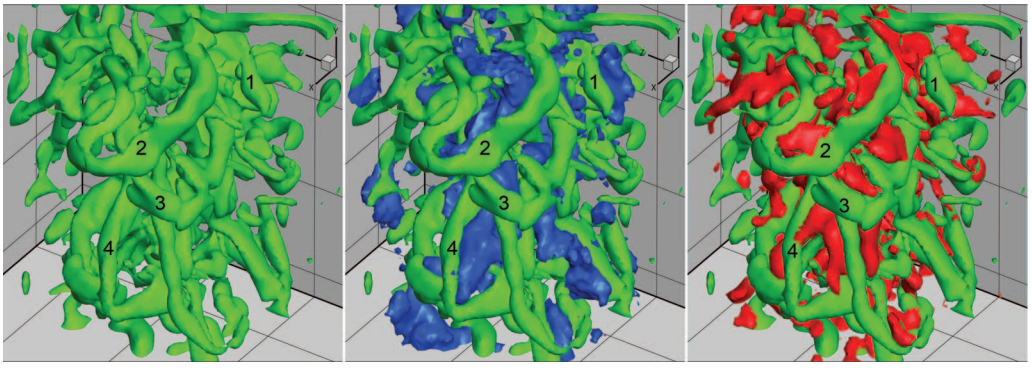

FIG. 19. Instantaneous production, P_{inst}, and dissipation, ϵ_{inst}, of turbulence kinetic energy in the vicinity of the vortical loops for $Re = 2640$. The loops are visualized with $\omega = 11\mathrm{s}^{-1}$ (shown in green). Intense production, presented here with iso-surfaces of $P_{inst} = 5 \times 10^{-5}\ \mathrm{m}^2/\mathrm{s}^3$ (shown in blue) is seen to occur in the center of the vortical loops (see loops numbered 1,2,3,4) in regions of strong vortex induction. Intense dissipation (iso-surfaces of $\epsilon_{inst} = 1.4 \times 10^{-5}\ \mathrm{m}^2/\mathrm{s}^3$ shown in red) is also large in between the legs of the loops (loops numbered 2,3,4). The high levels of production and dissipation in general occur quite close to the loops and appear to embrace the intense vorticity iso-surfaces.

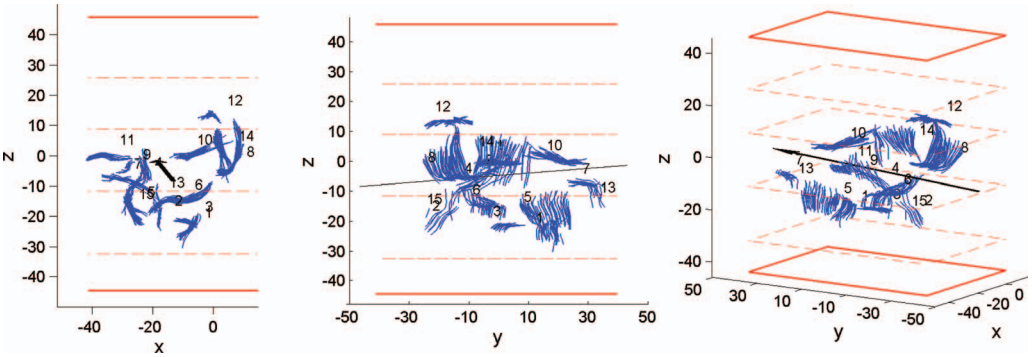

FIG. 20. Distribution of 15 extracted vortex cores (numbered) from $Re = 5280$ data. The cores are followed over a 40 time step interval. The mean flow axis is displayed with a black arrow. The panels show two perpendicular views and one perspective view of the same collection of cores. The interfaces between each reconstructed scanning volume are shown with broken red rectangles while the solid rectangles lines represent the extent of the domain.

Once a candidate structure has been chosen this process is repeated over a desired time interval or until the structure breaks down or leaves the volume. Figure 20 shows the result of applying the tracking algorithm to a 40 time step interval of $Re = 5280$ data. Most of the intense vortical structures identified exist in the vicinity of the jet core.

Figure 21(a) shows results of the application of the tracking algorithm to a single structure. This tube-like structure oriented transverse to the flow direction is tracked over the course of 12 time steps. For clarity, the structure is visualized in alternating colors for each time step. The visualized iso-surfaces define the boundary separating points above and below the vorticity magnitude threshold. For this data set, structures were typically tracked over around 700–850 ms, which corresponds to 4–5 eddy turn-over time scales of the structures ($D_{struct}/u_{rms} \sim 170$ ms) before they break up into smaller vorticity *blobs* and cannot be followed by our tracking algorithm. This structure duration is a lower bound, as they frequently advect into the volume, or are already present in the first time step. In some of the fast-scan data sets, structures have been tracked over as many as 120 time steps.

To highlight the advantage of the scanning-TPIV approach, the interfacial plane between adjacent reconstructed scanning volumes is also included in the visualization of the structure as a broken

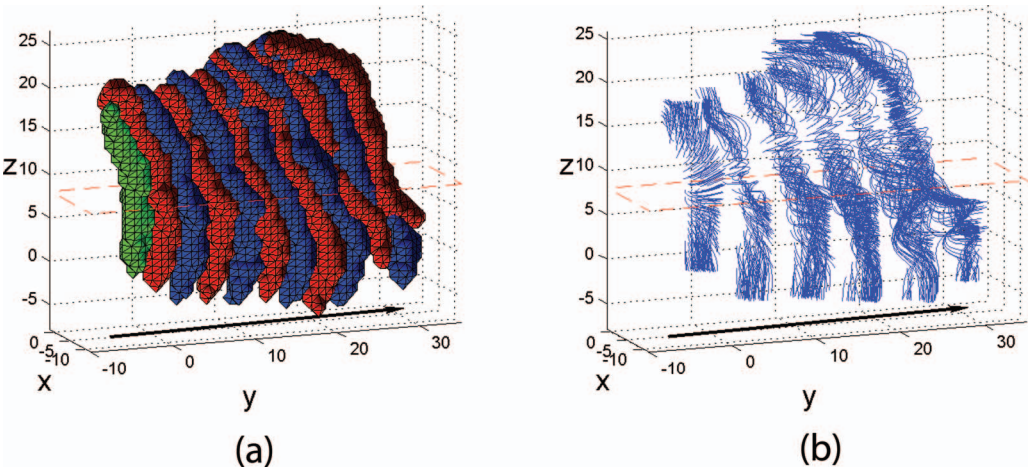

FIG. 21. (a) Visualization of the evolving shape of a tube-like structure for 12 consecutive time steps for $Re = 2640$ data. The structure is advecting from left to right with the green structure indicating the first in the sequence followed by alternating red and blue for clarity. (b) Streamlines of the fluctuating component of the velocity field for the evolving structure. The dashed lines indicate the interface separating two scanning volumes while the solid black arrow indicates the direction of the axial mean flow.

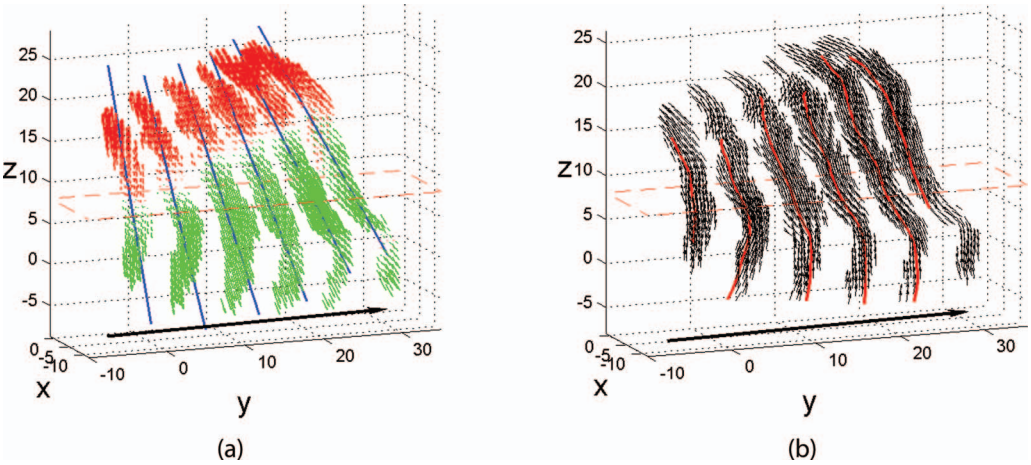

FIG. 22. (a) The fluctuating component of velocity projected onto the structure axis. The red and green vectors are in exactly opposite directions. (b) Vorticity vectors within the structure with a single vortex line displayed for each snapshot (red curves).

red rectangle. This interface divides this particular structure approximately at its mid-point showing a continuous transition between the individual laser-scanning volumes. The increased depthwise extent achievable using the scanning approach thus allows for tracking the trajectories of structures over a large spatial extent, which is especially useful for flows where motions may not strictly follow a single dominant flow direction.

Having identified the same structure over 12 consecutive time steps, it is now possible to analyze the different properties of its evolution. Figure 21(b) shows streamlines of the instantaneous fluctuating component of the velocity (the mean flow has been subtracted). Only every second snapshot of the evolution is visualized for clarity. In the first snapshot, the streamlines show that the fluctuating velocity is oriented parallel to the axis of the structure at its extremities and is roughly azimuthal at its midpoint, suggesting an inflection of the flow direction at the midpoint. As the structure evolves the azimuthal fluctuating velocity intensifies as evidenced by an increasingly swirling orbit of the streamlines about the structure axis. In the final snapshot of this sequence, the streamline orbits have a much higher curvature, suggesting that the degree of swirl has increased even further.

To investigate the nature of the velocity field fluctuations in this structure, the component parallel to the structure axis was extracted. Figure 22(a) shows the velocity fluctuation projected onto an approximation of the structure axis. This axis is approximated as a best fit 3D line through the data points and is calculated using principal component analysis. The projection confirms that the velocity fluctuation field is strongly axial (relative to the structure) at its ends and changes sign close to its midpoint. Figure 22(b) shows the corresponding vorticity vectors for every point within the structure. The vectors are oriented almost entirely axially as evidenced by the vortex lines (red curves) which pass through the structure centroid and faithfully follow the structure curvature.

In Sec. IV A, regions of $Q > 0$ was proposed as a potential criterion for extracting coherent structures from the 3D velocity field as this indicates the local dominance of rotation over strain. Soria *et al.*[48] investigated the geometry of dissipating motions in DNS data of incompressible mixing layers by comparing the principal invariants of the velocity gradient tensor. For an incompressible flow, the first principal invariant, P, is identically zero by continuity of the velocity field. The authors present an invariant map of the possible flow topologies that can occur in the $P = 0$ plane to illustrate the various dynamical configurations that correspond to correlation between the second and third principal invariants, denoted by Q and R, respectively. A discriminant line divides the map into regions of real and complex eigenvalues of the velocity gradient tensor, where complex eigenvalues imply a locally spiraling or closed streamline pattern for the velocity field in a frame following the structure (i.e., corresponding to positive Δ values). For regions of the flow where the local topology is dominated by stable-focus vortex stretching, the corresponding correlated behavior of

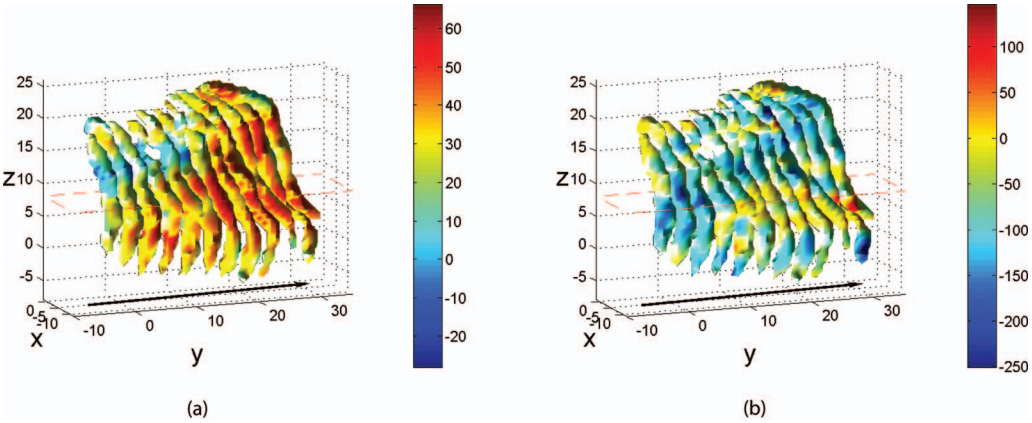

FIG. 23. Vorticity iso-surfaces, $\omega = 13.5\ \mathrm{s}^{-1}$, colored by the invariants of the velocity gradient tensor. (a) Second invariant, Q [s^{-2}], and (b) third invariant, R [s^{-3}].

the invariants suggests a local $Q > 0$, $R < 0$ event, while $Q > 0$, $R > 0$ events correspond to the case of unstable-focus compression. For our evolving structure, Figs. 23(a) and 23(b) show plots of thresholded vorticity magnitude colored by the instantaneous values of Q and R, respectively. The value of Q is strongly positive over almost the entirety of the structure during its evolution while R is also almost entirely negative over this interval, suggesting that it is undergoing stable-focus stretching. Some regions of the structure in the final frame exhibit some locally positive values of R indicating that this part of the structure may be experiencing unstable-focus compression as a prelude to its eventual break-up.

Visualization of regions of stable-focus stretching and unstable-focus compression has previously been performed by Ooi *et al.*[49] using DNS data from a simulation of forced isotropic turbulence. The authors noticed that regions of stable-focused stretching are generally elongated, similar to the tubes in our results, while the unstable-focused compression typically occurs at the ends of structures or where the structure bends. This latter observation is consistent with the final structure in the evolution presented in Fig. 23(b) where $R > 0$ at the ends of the structure and is at a local maximum at a location where a bend is observed.

D. Coherent structure evolution – High rate of temporal sampling

Following the procedure outlined above, the tracking was applied to a higher Reynolds number data set ($Re = 5280$) where particle images were acquired using the *fast-scan* protocol. This allows for a much higher sampling rate in exchange for limiting the total time duration of the experiment. The tracking algorithm was applied to the resulting vector data and the data for two separate structures is detailed herein. In order to contrast the dynamics of structures with differing orientation we present the evolution of a structure oriented roughly streamwise (Figs. 24(a) and 24(b)) and another structure oriented roughly azimuthally (Figs. 24(c) and 24(d)) with respect to the mean flow axes. The interfaces between the scanning volumes for both cases are included to highlight that the structures advect slightly across these interfaces at some point during their evolution, demonstrating the need for our scanning approach for capturing their full spatial extent.

The axially oriented structure is tracked over a 74 time step interval, and time-series plots of various quantities relating to its dynamics are presented in Figs. 25(a)–25(h). The time axis is non-dimensionalized as

$$\tau = t\left(\frac{r_{half}}{V_c}\right)^{-1}, \tag{6}$$

where t is the time coordinate and r_{half}/V_c is a flow time-scale representative of the large-scale motions, taking a value of 0.17 s for this Re. The structure centroid is located approximately

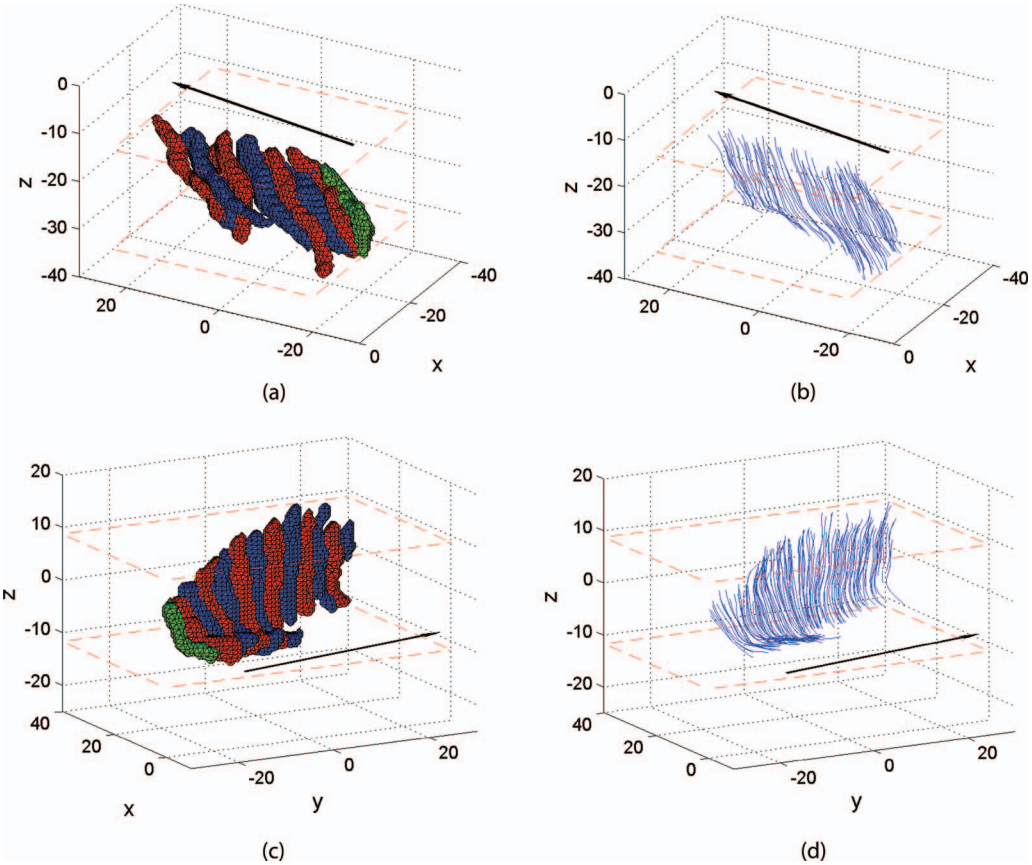

FIG. 24. Structure evolutions for the *fast-scan* case with a high degree of temporal sampling. (a),(b) A structure oriented roughly streamwise over a 74 snapshot interval (0.29 s) visualized using iso-vorticity and vortex lines, respectively. (c),(d) An approximately azimuthally oriented structure over a 125 snapshot interval (0.49 s) again visualized using iso-vorticity and vortex lines, respectively. The volume visualizations (a),(c) are restricted to every 10th time step for clarity.

half-way between the jet centerline and the jet half-width (Fig. 25(a)) where the mean axial velocity gradient in the radial direction is quite high (Fig. 10) and deviates little from this radial location over the course of its evolution. The orientation of the structure also remains approximately constant at a value of 37° relative to the streamwise axis (Fig. 25(b)). The mean value of the magnitude of the axial (black), radial (red), and azimuthal (blue) vorticity components within the structure is displayed in Fig. 25(c), while the mean magnitude of the vorticity vector is also presented (green) and remains quite constant over the entire evolution. The vorticity components recast in a frame local to the structure and the magnitudes of each component are presented in Fig. 25(d). As expected, the component of vorticity oriented parallel to the structure axis constitutes almost the entirety of the vorticity within the structure over its lifetime which agrees with the visualization of the vorticity vectors in Fig. 22(b) for the lower Reynolds number data. The evolving mean value of Q and R within the structure are displayed in Figs. 25(e) and 25(f), respectively. Q maintains a large positive value over the course of the evolution confirming that the structure is highly rotational while R initially exhibits a large negative value that decays to zero by the end of the snapshot series, after which the structure can no longer be tracked. This decay suggests a transition from stable-focused vortex stretching to the unstable focused vortex compression regime which may indicate the onset of structure instability and breakdown. Figure 25(g) shows the instantaneous contributions to production and dissipation, P_{inst} (blue) and ϵ_{inst} (red), which are defined as $P_{inst} = -u_i u_j \overline{S}_{ij}$ and $\epsilon_{inst} = 2\nu s_{ij} s_{ij}$, where index notation is used and u_i, s_{ij}, and $\overline{S}_{ij}$ are the instantaneous velocity fluctuation vector, the instantaneous rate of strain tensor and the mean rate of strain tensor, respectively. P_{inst} varies greatly over the evolution but is typically 3–4 times larger in magnitude than ϵ_{inst} indicating

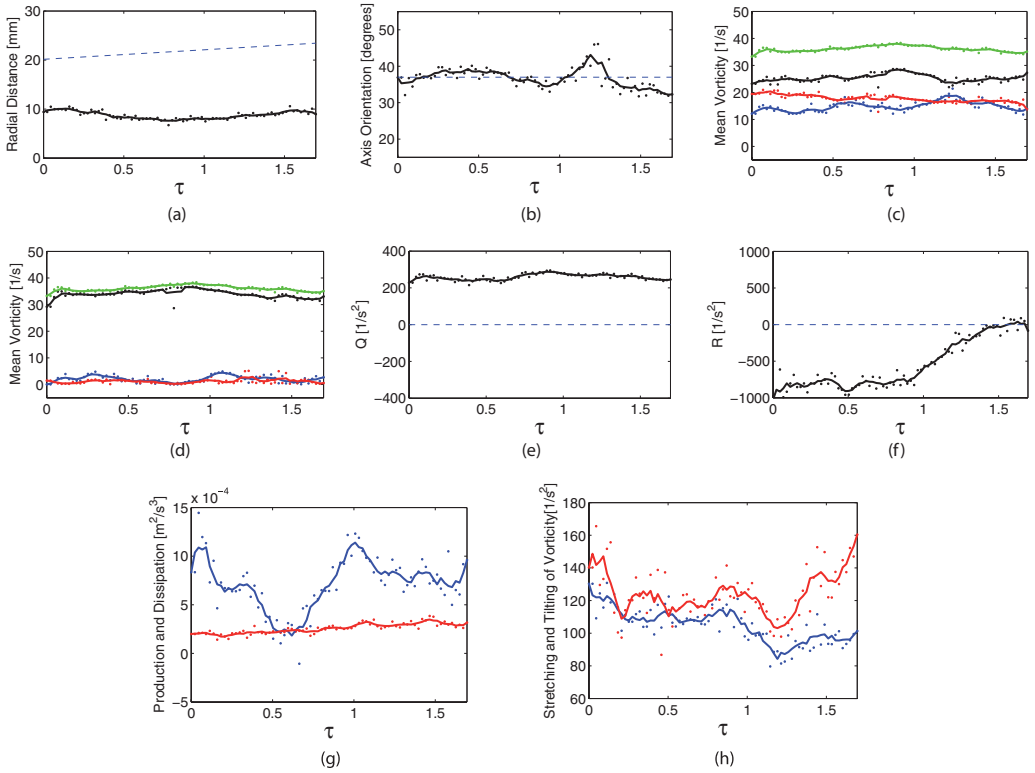

FIG. 25. Time evolution of flow quantities for an axially oriented structure tracked over 74 snapshots of the flow (a 0.29 s interval), where the time axis is replaced with the non-dimensional time, τ. The curves represent a five-point moving-average applied to the point data. (a) The radial distance of the structure centroid to the flow axis. The approximate jet half-width at the centroid of the advecting structure is shown as a dashed line. (b) The orientation of the structure axis relative to the mean flow axis. The dashed line indicates the approximately constant inclination of 37° relative to the mean flow axis. (c) Mean components of vorticity relative to the flow axes; radial, azimuthal, and axial (red, blue, and black, respectively). (d) Mean components of vorticity relative to the structure axis; radial, azimuthal, and axial (red, blue, and black, respectively). The green curves in (c) and (d) show the evolving mean vorticity magnitude within the structure over the interval. (e) Mean value of Q within the structure. (f) Mean value of R within the structure. (g) Time evolution of the instantaneous production (blue) and dissipation (red). (h) Time evolution of stretching (blue) and tilting (red).

that this structure is a net producer of turbulent kinetic energy over its lifetime. The orientation of the structure sets it up for stretching by the mean flow and as such the contribution of stretching and tilting to vorticity production inside the structure is of interest. The structure-averaged magnitudes of stretching and tilting are displayed in Fig. 25(h), where the contribution of each in the source term in the vorticity equation are, respectively,

$$Stretching = \big((\boldsymbol{\omega}\cdot\nabla)\,\mathbf{V}\cdot\boldsymbol{\omega}\big)\hat{\boldsymbol{\omega}}, \tag{7}$$

$$Tilting = (\boldsymbol{\omega}\cdot\nabla)\,\mathbf{V}\times\hat{\boldsymbol{\omega}}, \tag{8}$$

where $\hat{\boldsymbol{\omega}}$ is the unit vorticity vector.

For comparison, the time series of these quantities are again generated for the 125 consecutive snapshots of the azimuthally oriented structure in Figs. 24(c) and 24(d). This structure is located slightly outside the jet half-width and its centroid roughly maintains this radial distance from the flow axis (Fig. 26(a)). The axis of the structure is initially oriented approximately 70° to the flow axis but over the course of 1.5 flow times, τ, has relaxed to being almost perfectly orthogonal and maintains this orientation for the remainder of its evolution. The mean magnitude of the vorticity components within the structure as cast in the jet-coordinate system are initially almost equal (Fig. 26(c)) but as the structure tilts further away from the flow axis and towards the azimuthal

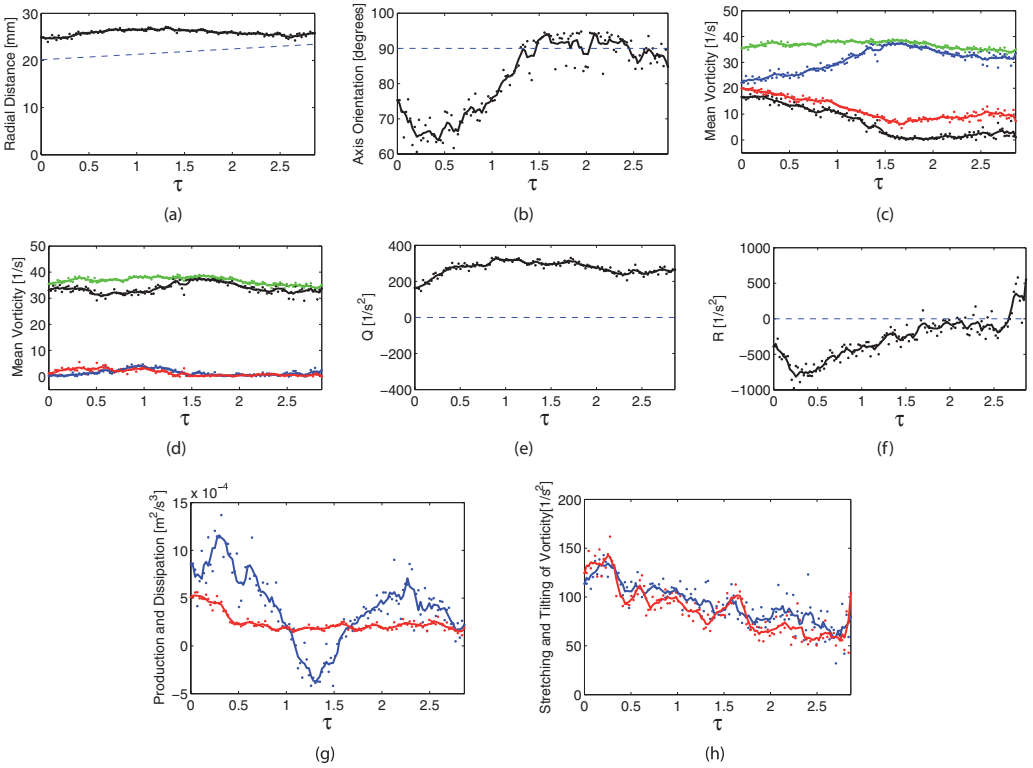

FIG. 26. Time evolution of flow quantities for an axially oriented structure tracked over 125 snapshots of the flow (a 0.49 s interval), where the time axis is replaced with the non-dimensional time, τ. The curves represent a five-point moving-average applied to the point data. (a) The radial distance of the structure centroid to the flow axis. The approximate jet half-width at the centroid of the advecting structure is shown as a dashed line. (b) The orientation of the structure axis relative to the mean flow axis. The structure relaxes to an orientation approximately orthogonal to the mean flow axis (see dashed line). (c) Mean components of vorticity relative to the flow axes; radial, azimuthal, and axial (red, blue, and black, respectively). (d) Mean components of vorticity relative to the structure axis; radial, azimuthal, and axial (red, blue, black, and respectively). The green curves in (c) and (d) show the evolving mean vorticity magnitude within the structure over the interval. (e) Mean value of Q within the structure. (f) Mean value of R within the structure. (g) Time evolution of the instantaneous production (blue) and dissipation (red). (h) Time evolution of stretching (blue) and tilting (red).

direction the azimuthal component becomes dominant, which is consistent with Fig. 26(d) confirming that the vorticity within the structure is oriented almost entirely with the axis of the structure. Q and R behave similarly as in the case of the axially oriented structure, although R can be seen to become considerably positive in the last snapshots of the time series. This indicates that the instability introduced by vortex compression may take longer to break down this structure as the direction of this compression does not coincide with any strong mean gradients as in the case of the axial structure. Dissipation (Fig. 26(g)) appears to be approximately the same as in the case of the axial structure, while production is initially large as the structure is tilting but decreases rapidly as it tilts further away from the axis and relaxes to its final orientation, even being briefly negative at which point energy is transferring from the turbulent scales to the mean flow. Figure 26(h) shows that both tilting and stretching decay steadily over the course of the evolution.

Owing to the large time series acquired for the azimuthally oriented structure using the *fast-scan* protocol, it is possible to generate ensemble statistics pertaining to this structure alone for comparison with already existing data for the turbulent round jet. Khashehchi *et al.*[11] used TPIV to analyze the invariants of the velocity gradient tensor following Soria *et al.*[48] in order to qualify the local topology in both the turbulent region of the jet and in the vicinity of the turbulent non-turbulent interface by using conditional sampling. For comparison with our data, we firstly present the invariant maps calculated over the 125 consecutive snapshots of the entire flow where the azimuthal structure is present. Following Khashehchi *et al.*,[11] Fig. 27(a) shows joint PDFs of invariants of the velocity

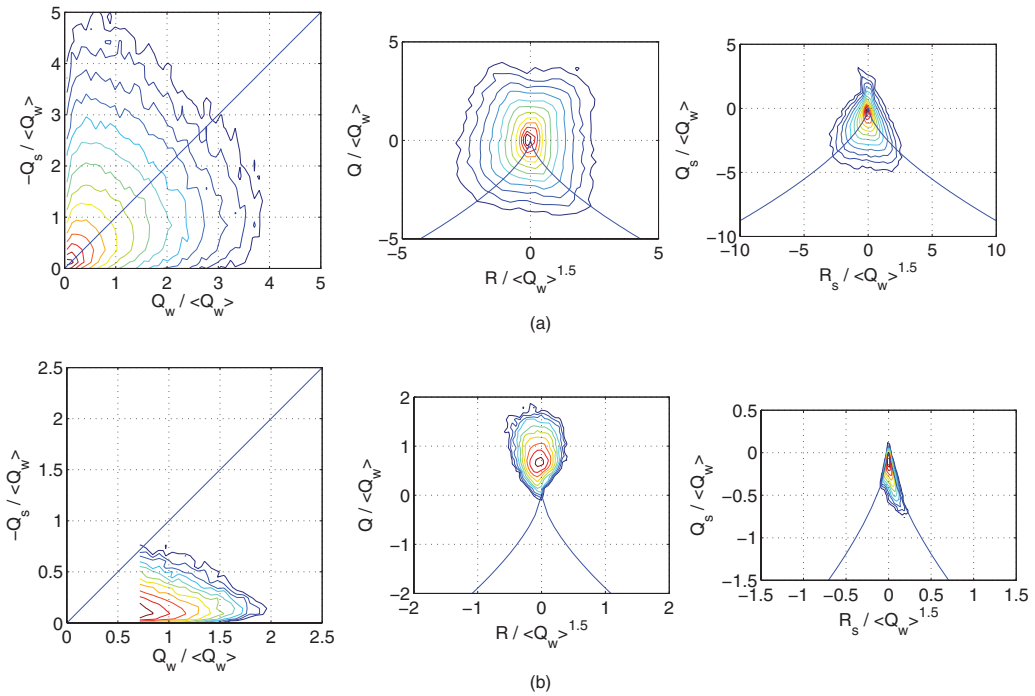

FIG. 27. (a) Velocity gradient tensor invariant maps calculated using the entire domain ensemble over a 125 snapshot interval of the evolving flow. 14 contour levels of the joint PDF are displayed, ranging logarithmically with exponents equally spaced from (left to right) −5 to 1, −6 to −1, and −6 to −1, respectively. (b) Velocity gradient tensor invariant maps calculated for a single coherent structure over a 125 snapshot interval of the evolving flow. 10 contour levels of the joint PDF are displayed, ranging logarithmically with exponents equally spaced from (left to right) −2 to 2, −3 to 2, and −1 to 4, respectively.

gradient tensor, the rate of strain tensor and the spin tensor where every point in the domain has been included in the sample. The velocity gradients were calculated as in Sec. II E, by differencing the velocity averaged over the surfaces of cubes matched to the correlation window size. The joint PDF of the second invariants of the rate of strain tensor (Q_s) and the spin tensor (Q_w) is approximately symmetric about the 45° line. For this PDF, the vertical axis represents regions of flow with zero enstrophy and a high degree of dissipation of turbulent kinetic energy while the horizontal axis represents regions of high enstrophy and low dissipation. The 45° line is a balance between both axes and typically corresponds to highly dissipative and enstrophic vortex sheets. Our data agree quite well with data conditioned on being inside the turbulent region of the jet.[11] The joint PDF of Q and R is close to symmetric about both axes. This indicates the presence of both enstrophic stretched and compressed vortices and also stable and unstable shear corresponding to irrotational fluid. The inclusion of both highly rotational and irrotational regions in our sample in addition to the limited statistical convergence of the time series data (i.e., the ensemble is generated over a rather short time interval of the data) makes it difficult to identify any preferred correlation of the invariants, although existing results show that a skewness towards $Q > 0$, $R < 0$ and $Q < 0$, $R < 0$ events are indicative of turbulent shear layer flow.[48] The joint PDF of the second and third invariants of the rate of strain tensor (Q_s and R_s, respectively) shows very slight skewness toward $R_s > 0$ for largely negative Q_s where for turbulent flow the data is expected to be strongly correlated in this quadrant.[48] The absence of strong skewness can be attributed both to insufficient statistical convergence of the joint PDF and also to the under resolution of the spatial length scales of the flow. Data lying above the discriminant line separating complex and real eigenvalues of the velocity gradient tensor are the result of divergence error in our data, which was investigated in an earlier section, and our results are consistent with ensemble TPIV data for turbulent jet flow by Khashehchi *et al.*[11] These errors have also been systematically studied by Buxton *et al.*[50] and Worth *et al.*,[13]using both high-resolution numerical simulations and experiments. The shape of the joint distribution in the center panel of Figure 27(a) has only a very weak tail in the teardrop shape (compare with Figure 11 of Buxton

et al.[50]), which is indicative of noise in the velocity gradients, used to compute the invariants Q and R. It would be of future interest to apply our technique at higher image magnifications to try to reduce this noise in the gradients.

The joint PDFs detailed above were then recomputed for the 125 snapshots of the time series where the sample is restricted to points within the coherent structure only. This approach can be considered as a conditional sample where the condition is 'existence within a single evolving coherent structure' over the time interval considered. The data is presented in Fig. 27(b). The joint PDF of Q_s and Q_w is skewed heavily towards the Q_w axis indicating that the structure is highly enstrophic and weakly dissipative (i.e., weakly strained), which is a result that is easily seen in the time series data for this structure in Figs. 26(d) and 26(g). The data is cut off sharply at a certain value of Q_w due to the fact that Q_w is proportional to enstrophy density. Since vorticity thresholding was applied to the data set for the original vortex identification procedure then Q_w will also inevitably be thresholded. The joint PDF of Q and R is confined essentially entirely to $Q > 0$ and is anchored to the origin, indicating that this is an enstrophy dominated structure undergoing little strain. The joint PDF of Q_s and R_s is skewed towards $R_s > 0$ and is highly peaked at the origin, again indicating that irrotational straining is negligible within this particular structure.

V. DISCUSSION AND CONCLUSIONS

A. The advantages and limitations

To conclude, we highlight the capabilities and drawbacks of this scanning technique. The strongest advantage is the large number of depthwise planes which can be accurately resolved, making measurements easier for large domain depths. This larger resolution in the depth, achieved without sacrificing transverse spatial resolution, transforms conventional TPIV results from volume slices, to more cubical domains. The total number of adjacent volumes is perhaps only limited by the particle seeding density, where attenuation of the particle-scattered light becomes excessive if it must travel through too dense a particle field to reach the cameras. In some flow configurations this limitation can be overcome or minimized by selectively seeding the flow volume of interest. For the jet, a weakly co-flowing configuration could provide seeding particles directly to the turbulent region of the jet as well as the superlayer, leaving the rest of the water tank free of particles.

The galvanometer can accommodate a range of different input signals allowing for a variety of different image acquisition strategies. For example, where each mirror position is pulsed multiple times to facilitate the possible calculation of higher order time derivatives, interpolation in time or correlation signal averaging in time to achieve a higher signal-to-noise ratio.[12,51]

Other practical advantages of the scanning approach include the optimization of laser energy. By focusing each laser pulse in a smaller volume, the particle scattering is brighter and one can use smaller lens apertures, which in turn allows for larger depth of focus.

One drawback of the technique, is the slight time delay between the adjacent volumes, which causes some tilting and deformation of the flow structures, presented during each time step. This is less important for the *fast-scan* procedure where the time delay can be reduced, only being limited by the maximum frame-rate of the high-speed cameras. In the case of the *double-pulse* procedure, the deformation of the reconstructed flow field might be significant if the scanning speed is not fast enough. From our data the streamwise velocity in the test section is <0.3 m/s and time delay between volumes is always less than 4.4 ms, for the *double-pulse* protocol. This gives relative shifting of less than 1.3 mm, between adjacent volumes. Therefore, the average distortion on each side of the jet, can be approximated by about 3.5 mm, which is only of the order of one correlation window size. This can potentially be corrected for by interpolation in time. Another way of characterizing the deformation is the ratio of the mean axial convection velocity of the structures in the flow field, to the traveling speed of the light sheet. In the present study, this ratio is approximately 5.6% (5 planes at $Re = 10\,700$), resulting in insignificant distortion effects on the topology of the coherent structures. For the fast-scan protocol, this ratio is much smaller at about 0.5% for $Re = 2640$.

If we limit our scanning to only two volumes, this space deformation can be entirely eliminated, by frame-straddling of the laser pulses, across two adjacent video frames.

B. Future directions

The proposed scanning modification of tomographic-PIV is well positioned to take advantage of future improvements in video imaging technology, as it can easily expand with the increased frame-rates and pixel counts of high-speed CMOS sensors, which is occurring at a steady pace.[52] For perspective, herein we use between 160 and 288 Mpx of image information to calculate each velocity volume, i.e. 4 Mpx/frame; 4 cameras; 5-9 volumes; for 2 laser pulses. When larger and faster sensors come online, this technique can be applied to an even larger spatial extend, or to flow at larger Reynolds numbers.

Wide application of TPIV is currently hampered by the large computational cost, most of which is devoted to the evaluation of the 3D correlations. However, TPIV time-series are naturally vectorizable on large computer clusters, as each time step is independent of all the others, thereby only occupying one node, with sufficient memory size. Dedicated GPU architectures should also speed up these calculations. Furthermore, novel methods of rapidly calculating the 3D correlations based on de-scaled reconstructed volume data which exploit the sparseness of the data, are now being developed and could speed up these calculations by an order of magnitude.[53] When the turn-over time of TPIV time-series calculations is significantly reduced one can see numerous applications emerge, such as experimental optimization of turbulent flow-control strategies for mixing or drag reduction.[54]

Herein we have demonstrated the promise of this scanning technique. Due to the novel approach for exceeding the inherent spatial limitation of regular TPIV, coupled with ongoing improvements in algorithms and chip hardware, scanning tomographic PIV (STPIV) could become the future logical technique of choice for general laboratory studies of turbulent flows.

However, a major inherent drawback of all scanning techniques is the unavoidable flow evolution which occurs during the scanning. This limits the smallest dynamic time-scales which can be studied, which in turn limits the turbulent *Re*. Furthermore, the much smaller kinematic viscosity for liquids than gas, limits us to liquids as the working medium. For the foreseeable future, this technique can therefore not be used in high *Re* gas flows.

[1] G. E. Elsinga, F. Scarano, B. Wieneke, and B. W. Van Oudheusden, "Tomographic particle image velocimetry," Exp. Fluids **41**, 933–947 (2006).
[2] N. A. Worth and T. B. Nickels, "Acceleration of Tomo-PIV by estimating the initial volume intensity distribution," Exp. Fluids **45**, 847–856 (2008).
[3] C. Atkinson and J. Soria, "An efficient simultaneous reconstruction technique for tomographic particle image velocimetry," Exp. Fluids **47**, 553–568 (2009).
[4] C. Atkinson, S. Coudert, J. M. Foucaut, M. Stanislas, and J. Soria, "The accuracy of tomographic particle image velocimetry for measurements of a turbulent boundary layer," Exp. Fluids **50**, 1031–1056 (2011).
[5] D. H. Barnhart, R. J. Adrian, and G. C. Papen, "Phase-conjugate holographic system for high-resolution particle-image velocimetry," Appl. Opt. **33**, 7159–7170 (1994).
[6] J. Zhang, B. Tao, and J. Katz, "Turbulent flow measurement in a square duct with hybrid holographic PIV," Exp. Fluids **23**, 373–381 (1997).
[7] T. Hori and J. Sakakibara, "High-speed scanning stereoscopic PIV for 3D vorticity measurement in liquids," Meas. Sci. Tech. **15**, 1067–1078 (2004).
[8] C. Brücker, "3D scanning-particle-image-velocimetry: Technique and application to a spherical cap wake flow," Appl. Sci. Res. **56**, 157–179 (1996).
[9] F. Scarano and C. Poelma, "Three-dimensional vorticity patterns of cylinder wakes," Exp. Fluids **47**, 69–83 (2009).
[10] A. Schröder, R. Geisler, G. E. Elsinga, F. Scarano, and U. Dirkscheide, "Investigation of a turbulent spot and a tripped turbulent boundary layer flow using time-resolved tomograpahic PIV," Exp. Fluids **44**, 305–316 (2008).
[11] M. Khashehchi, G. E. Elsinga, A. Ooi, J. Soria, and I. Marusic, "Studying invariants of the velocity gradient tensor of a round turbulent jet across the turbulent/nonturbulent interface using Tomo-PIV," in *Proceedings of 15th International Symposium on Applications of Laser Techniques to Fluid Mechanics, Lisbon, Portugal, 05–08 July 2010*.
[12] D. Violato and F. Scarano, "Three-dimensional evolution of flow structures in transitional circular and chevron jets," Phys. Fluids **23**, 124104 (2011).
[13] N. A. Worth, T. B. Nickels, and N. Swaminathan, "A tomographic PIV resolution study based on homogeneous isotropic turbulence DNS data," Exp. Fluids **49**, 637–656 (2010).
[14] G. T. Herman and A. Lent, "Iterative reconstruction algorithms," Comput. Biol. Med. **6**, 273–294 (1976).
[15] D. Michaelis, M. Novara, F. Scarano, and B. Wieneke, "Comparison of volume reconstruction techniques at different particle densities," in *Proceedings of 15th International Symposium on Applications of Laser Techniques to Fluid Mechanics, Lisbon, Portugal, 05–08 July 2010*.
[16] G. E. Elsinga, J. Westerweel, F. Scarano, and M. Novara, "On the velocity of ghost particles and the bias errors in Tomographic-PIV," Exp. Fluids **50**, 825–838 (2011).

[17] S. Ghaemi and F. Scarano, "Multi-pass light amplification for tomographic particle image velocimetry applications," Meas. Sci. Technol. **21**, 127002 (2010).
[18] J. Kitzhofer and C. Brücker, "Tomographic particle tracking velocimetry using telecentric imaging," Exp. Fluids **49**, 1307–1324 (2010).
[19] J. Kitzhofer, C. Brücker, and O. Pust, "Tomo PTV using 3D scanning illumination and telecentric imaging," in *Proceedings of 8th International Symposium on Particle Image Velocimetry, Melbourne Australia, 25–28 August 2009*.
[20] N. Rajaratnam, *Turbulent Jets* (Elsevier Scientific, 1976).
[21] P. E. Dimotakis, R. C. Miake-Lye, and D. A. Papantoniou, "Structure and dynamics of round turbulent jets," Phys. Fluids **26**, 3185–3193 (1983).
[22] S. C. Crow and F. H. Champagne, "Orderly structure in jet turbulence," J. Fluid Mech. **3**, 547–591 (1971).
[23] I. Wygnanski and H. Fielder, "Some measurements in the self-preserving jet," J. Fluid Mech. **38**(3), 577–612 (1969).
[24] H. Schlichting, "Laminare Strahlenausbreitung," Z. Angew. Math **13**, 260–263 (1933).
[25] T. Matsuda and J. Sakakibara, "On the vortical structure in a round jet," Phys. Fluids **17**, 025106 (2005).
[26] B. Ganapathisubramani, K. Lakshminarasimhan, and N. T. Clemens, "Determination of complete velocity gradient tensor by using cinematographic stereoscopic PIV in a turbulent jet," Exp. Fluids **42**, 923–939 (2007).
[27] J. A. Mullin and W. J. A. Dahm, "Dual plane stereo particle image velocimetry of velocity gradient tensor fields in turbulent shear flow. I. Accuracy assessments," Phys. Fluids **18**, 035101-1–035101-18 (2010).
[28] K. Staack, R. Geisler, A. Schröder, and D. Michaelis, "3D-3C-coherent structure measurements in a free turbulent jet," in *Proceedings of 15th International Symposium on Applications of Laser Techniques to Fluid Mechanics, Lisbon, Portugal, 05–08 July 2010*.
[29] R. J. Adrian, "Stochastic estimation of conditional structure: A review," Appl. Sci. Res. **53**, 291–303 (1994).
[30] C. A. Friehe, C. W. Van Atta, and C. H. Gibson, "Jet turbulence: Dissipation rate measurements and correlations," AGARDograph **93**, 18-1–18-7 (1971).
[31] B. Wieneke, "Volume self-calibration for 3D particle image velocimetry," Exp. Fluids **45**, 549–556 (2008).
[32] F. Scarano and M. L. Riethmuller, "Advances in iterative multigrid PIV image processing," Exp. Fluids **29**, S51–S60 (2000).
[33] J. Westerweel and F. Scarano, "Universal outlier detection for PIV data," Exp. Fluids **39**, 1096–1100 (2005).
[34] S. K. Lele, "Compact finite difference schemes with spectral-like resolution," J. Comput. Phys. **3**(1), 16–42 (1992).
[35] R. J. Adrian and J. Westerweel, *Particle Image Velocimetry* (Cambridge University Press, New York, 2011).
[36] A. Fouras and J. Soria, "Accuray of out-of-plane vorticity measurements derived from in-plane velocity field data," Exp. Fluids **25**, 409–430 (1998).
[37] J. Soria, "Particle Image Velocimetry - Application to turbulence studies," *Lecture Notes on Turbulence and Coherent Structures in Fluids, Plasmas and Nonlinear Media*, edited by M. Shats and H. Punzmann (World Scientific, 2006), Vol. 4, pp. 309–348.
[38] S. Herpin, C. Y. Wong, M. Stanislas, and J. Soria, "Stereoscopic PIV measurements of a turbulent boundary layer with a large spatial dynamic range," Exp. Fluids **45**, 745–763 (2008).
[39] S. Tokgoz, G. E. Elsinga, R. Delfos, and J. Westerweel, "Spatial resolution and dissipation rate estimation in Taylor-Couette flow for tomographic PIV," Exp. Fluids **53**, 561–583 (2012).
[40] C. O. Pasehereit, D. Oster, T. A. Long, H. E. Fiedler, and I. Wygnanski, "Flow visualization of interactions among large coherent structures in an axisymmetric jet," Exp. Fluids **12**, 189–199 (1992).
[41] H. A. Becker and T. A. Massaro, "Vortex evolution in a round jet," J. Fluid Mech. **31**(3), 435–448 (1967).
[42] D. Liepmann and M. Gharib, "The role of streamwise vorticity in the near-field entrainment of round jets," J. Fluid Mech. **245**, 643–668 (1992).
[43] M. S. Chong, A. E. Perry, and B. J. Cantwell, "A general classification of three-dimensional flow fields," Phys. Fluids A **2**, 765–777 (1990).
[44] J. Jeong and F. Hussain, "On the identification of a vortex," J. Fluid Mech. **285**, 69–94 (1995).
[45] J. C. R. Hunt, A. A. Wray, and P. Moin, "A general classification of three-dimensional flow field," Center for Turbulence Research Report No. CTR-S88, p. 163, 1988.
[46] N. A. Worth and T. B. Nickels, "Time-resolved volumetric measurement of fine-scale coherent structures in turbulence," Phys. Rev. E **84**, 025301(R) (2011).
[47] F. J. Diez, Y. Cheng, and A. Villegas, "Time resolved visualization of velocity gradients measured with near Kolmogorov-scale resolution in turbulent shear flows," Exp. Therm. Fluid Sci. **35**(6), 1223–1229 (2011).
[48] J. Soria, R. Sondergaard, B. J. Cantwell, M. S. Chong, and A. E. Perry, "A study of finescale motions of incompressible time developing mixing layers," Phys. Fluids **6**, 871–884 (1994).
[49] A. Ooi, J. Martin, J. Soria, and M. S. Chong, "A study of the evolution and characteristics of the invariants of the velocity-gradient tensor in isotropic turbulence," J. Fluid Mech. **381**, 141–174 (1999).
[50] O. R. H. Buxton, S. Laizet, and B. Ganapathisubramani, "The effects of resolution and noise on kinematic features of fine-scale turbulence," Exp. Fluids **51**, 1417–1437 (2011).
[51] C. D. Meinhart, S. T. Werely, and J. G. Santiago, "A PIV algorithm for estimating time-averaged velocity fields," J. Fluids Eng. **122**, 285–289 (2000).
[52] S. T. Thoroddsen, T. G. Etoh, and K. Takehara, "High-speed imaging of drops and bubbles," Annu. Rev. Fluid Mech. **40**, 257–285 (2008).
[53] D. Michaelis, private communication (2012).
[54] P. J. Schmid, L. Li, M. P. Juniper, and O. Pust, "Decomposition of experimental data into dynamic modes," Theor. Comput. Fluid Dyn. **25**(1), 249–259 (2011).